AFRL-AFOSR-VA-TR-2020-0042

Structure and Dynamics of Highly Turbulent, Interacting Flames

Jacqueline O'Connor
PENNSYLVANIA STATE UNIVERSITY

11/29/2019
Final Report

Air Force Research Laboratory
AF Office Of Scientific Research (AFOSR)/ RTA1
Arlington, Virginia 22203
Air Force Materiel Command

REPORT DOCUMENTATION PAGE

Form Approved
OMB No. 0704-0188

1. REPORT DATE *(DD-MM-YYYY)*	2. REPORT TYPE	3. DATES COVERED *(From - To)*
21-05-2020	Final Performance	01 Dec 2015 to 31 Aug 2019

4. TITLE AND SUBTITLE
Structure and Dynamics of Highly Turbulent, Interacting Flames

5a. CONTRACT NUMBER

5b. GRANT NUMBER
FA9550-16-1-0075

5c. PROGRAM ELEMENT NUMBER
61102F

6. AUTHOR(S)
Jacqueline O'Connor

5d. PROJECT NUMBER

5e. TASK NUMBER

5f. WORK UNIT NUMBER

7. PERFORMING ORGANIZATION NAME(S) AND ADDRESS(ES)
PENNSYLVANIA STATE UNIVERSITY
201 OLD MAIN
UNIVERSITY PARK, PA 16802-1505 US

8. PERFORMING ORGANIZATION REPORT NUMBER

9. SPONSORING/MONITORING AGENCY NAME(S) AND ADDRESS(ES)
AF Office of Scientific Research
875 N. Randolph St. Room 3112
Arlington, VA 22203

10. SPONSOR/MONITOR'S ACRONYM(S)
AFRL/AFOSR RTA1

11. SPONSOR/MONITOR'S REPORT NUMBER(S)
AFRL-AFOSR-VA-TR-2020-0042

12. DISTRIBUTION/AVAILABILITY STATEMENT
A DISTRIBUTION UNLIMITED: PB Public Release

13. SUPPLEMENTARY NOTES

14. ABSTRACT
The overall objective of this program was to develop a fundamental understanding of the structure and dynamics of highly turbulent, interacting flames. Flame interaction occurs in a wide range of combustion applications of interest to the Department of Defense, and as flame interaction can introduce additional flame physics to turbulent flames, it is an important addition to the research portfolio focusing on turbulent flame behavior. The key learnings from this program are:
Implementation and publication of a methodology for rigorously identifying flame interaction events and their characteristics from high-speed PLIF images
Quantification of flame interaction event occurrence frequencies and how impactful these events are on the flame surface and its area
Identification of the role that the flow field plays in determining flame interaction statistics and topology
Differentiation of flame interaction statistics for different flame shapes, including Bunsen flames and V-flames
Quantification of the impact of pocket formation on flame area dynamics and flame speeds
Identification of the role of piloting on local flame dynamics and flame structure
Development of a method for estimating the influence of out-of-plane errors on planar flame measurements
The results of this study have several implications for the future of turbulent flame research. First, flame interactions affect a non-negligible amount of the flame surface of a turbulent flame and can result in significant losses and additions of flame area at any given time. However, many of these interactions are happening on length scales smaller than the Taylor microscale of the incoming turbulent flow, indicating that these interactions need to be accounted for at the sub-grid scale. Second, the frequency and characteristics of the interactions are highly dependent on flame shape and the hydrodynamic instabilit

15. SUBJECT TERMS
turbulent flame, turbulent combustion, flame propagation, flame topology, flame interaction

16. SECURITY CLASSIFICATION OF:			17. LIMITATION OF ABSTRACT	18. NUMBER OF PAGES	19a. NAME OF RESPONSIBLE PERSON
a. REPORT	b. ABSTRACT	c. THIS PAGE			LI, CHIPING
Unclassified	Unclassified	Unclassified	UU		19b. TELEPHONE NUMBER *(Include area code)* 703-696-8574

Standard Form 298 (Rev. 8/98)
Prescribed by ANSI Std. Z39.18

Final Report: Structure and Dynamics of Highly Turbulent, Interacting Flames
Grant FA9550-16-1-0075

PI: Dr. Jacqueline O'Connor, Pennsylvania State University
Graduate students: Ankit Tyagi (Ph.D. Fall 2019), Kaylyn Beseler (M.S. Fall 2019)
Undergraduate students: Mike Meehan, Ryan Shupp
Research engineer: Dr. Stephen Peluso, Pennsylvania State University
Collaborators: Dr. Isaac Boxx, DLR-Stuttgart; Dr. Peter Hamlington, CU-Boulder

1 Executive Summary

The overall objective of this program was to develop a fundamental understanding of the structure and dynamics of highly turbulent, interacting flames. Flame interaction occurs in a wide range of combustion applications of interest to the Department of Defense, and as flame interaction can introduce additional flame physics to turbulent flames, it is an important addition to the research portfolio focusing on turbulent flame behavior. Flame interaction can affect flame structure, flame propagation, flame static stability, flame dynamic stability, and emissions formation. While each of these issues is certainly important, the current proposal addresses the most foundational of these issues, which are flame structure and flame propagation in interacting flame environments. There were three main goals of the proposed work, all focused on developing a better understanding of flame interaction processes for the development of more accurate turbulent flame models:

Goal 1: Better understand flame interactions and how operational parameters – including turbulence intensity, turbulent length scales, turbulence anisotropy, Lewis number, and flame shape – alter flame interaction processes.

Goal 2: Determine the differences between flame-flame and turbulence-flame interactions, particularly the impact that flame-flame interactions have on key properties that determine flame structure and propagation, including flame area (or flame surface density), flame stretch, flame heat release rate, and combustion efficiency.

Goal 3: Describe the relative importance of flame-flame vs. turbulence-flame interaction processes on both local and global flame characteristics as a function of operating parameter to determine in what regimes it is critical to incorporate flame-interaction effects in combustion models.

Each of these goals has been achieved over the duration of this program. The key learnings from this program are:

- Implementation and publication of a methodology for rigorously identifying flame interaction events and their characteristics from high-speed PLIF images
- Quantification of flame interaction event occurrence frequencies and how impactful these events are on the flame surface and its area
- Identification of the role that the flow field plays in determining flame interaction statistics and topology
- Differentiation of flame interaction statistics for different flame shapes, including Bunsen flames and V-flames
- Quantification of the impact of pocket formation on flame area dynamics and flame speeds
- Identification of the role of piloting on local flame dynamics and flame structure
- Development of a method for estimating the influence of out-of-plane errors on planar flame measurements

The results of this study have several implications for the future of turbulent flame research. First, flame interactions affect a non-negligible amount of the flame surface of a turbulent flame and can result in significant losses and additions of flame area at any given time. However, many of these interactions are

happening on length scales smaller than the Taylor microscale of the incoming turbulent flow, indicating that these interactions need to be accounted for at the sub-grid scale. Second, the frequency and characteristics of the interactions are highly dependent on flame shape and the hydrodynamic instability characteristics of the underlying flow field. V-flame dynamics were found to have interactions that coupled with the periodicity of the flow field, whereas this was not the case in Bunsen flames. Third, the presence of back-support pilots can dramatically impact the results of any turbulent flame experiment. By creating an adiabatic shield around the flame, the back-support pilots make the flame insensitive to extinction, thereby changing its dynamical behavior. Finally, a method for estimating the role of out-of-plane effects on planar measurements of flame behavior has been developed and used to estimate uncertainty in the measurements taken over the course of this project. The remainder of this report discusses the detailed results that support each of the seven key learnings from this program.

2 Flame interaction identification

2.1 Publications from this effort

- Tyagi, A., Boxx, I., Peluso, S., & O'Connor, J. (2019) "Statistics and topology of local flame-flame interactions in turbulent flames," *Combustion and Flame*, **203**, p. 92-104

2.2 Flame interaction identification methodology

The goal of this work is to experimentally characterize the frequency and topology of local flame-flame interaction events at a range of operating conditions in both single- and dual-flame configurations in a modular burner experiment. High-speed planar laser induced fluorescence (PLIF) was used to measure the distribution of the hydroxyl combustion radical in the post-combustion products; the flame edge is extracted from these images. The OH-PLIF images are binarized using a dynamic thresholding technique that reduces the sensitivity of the calculation to intensity variations in each frame. A non-rigid image registration technique is utilized to identify local flame-flame interaction events. This technique estimates non-uniform displacement fields to perform image alignment between two binarized OH-PLIF images. Figure 1 illustrates the application of image registration on the OH-PLIF data for the current study. In this technique, operations are performed on binarized OH-PLIF images to estimate the displacement of flame edges between two consecutive images ('fixed' and 'moved'). Here, 'fixed' image refers to the image at any time of interest t_0 and 'moved' image refers to the consecutive image at time $t_0 + \Delta t$. The displacement field matches different features of flame edges between the two images and accounts for the local convection in the flow field, as highlighted in Figure 1(b). Translation operations are performed on the 'moved' image such that all common features of the 'fixed' and 'moved' images are matched (Figure 1(c)) and resulting differences are recorded, which correspond to topological differences in these flames within Δt. An example of such a difference is shown in Figure 1(d). Figure 1(e) and (f) show a time-sequence of unregistered and registered images.

In correctly utilizing this technique for identifying interactions in flames, an estimation of the displacement field for the 'moved' image is required. This estimation depends on the number of iterations and pyramid levels used in the algorithm. Here, the pyramid levels correspond to the levels of resolution (coarse-to-fine) utilized for alignment of flame edge features. For high turbulence flames, strong flame wrinkling occurs over a range of scales and the use of multi-resolution displacement field estimation is important for robust image alignment. Depending on the bulk flow velocities of the flames, the pyramid levels utilized for image registration vary from three to seven for cases in this study. These pyramid levels are selected by individually checking for convergence of the displacement fields for each case.

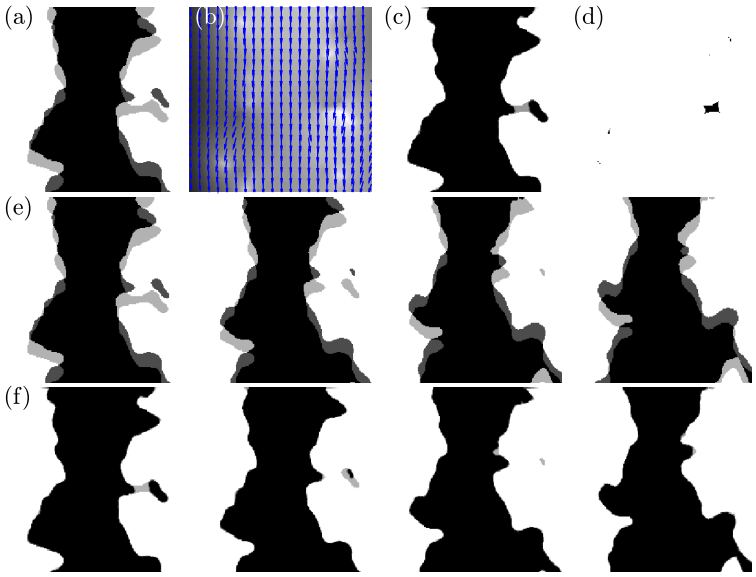

Figure 1: Image registration methodology in identification of flame-flame interactions: (a) unregistered 'moved' image plotted on the 'fixed' image for two consecutive images, (b) vectors associated with displacement field for the 'moved' image plotted on the absolute displacement for each pixel in the image, (c) registered 'moved' image plotted on the 'fixed' image, and (d) differences between registered 'moved' and 'fixed' images. Time-series of (e) unregistered and (f) registered image pairs

Schematics of interaction events identified from the image registration technique are shown in Figure 2. Once consecutive binarized OH-PLIF images are registered, they are subtracted to search for non-zero regions that correspond to topological changes occurring within 100 µs. Edges of the non-zero regions (regions with hashed pattern in Figure 2) are evaluated and decomposed into L_- and L_+. Here, L_- identifies the part of the flame edge that is consumed due to the interaction event and L_+ is the part that remains on the connected flame edge after the interaction occurs. For all non-zero regions identified, comparisons between the arc-lengths of L_- and L_+ are made to ensure only flame surface reduction events are captured. These post-processing steps are taken for both reactant- and product-side interactions separately.

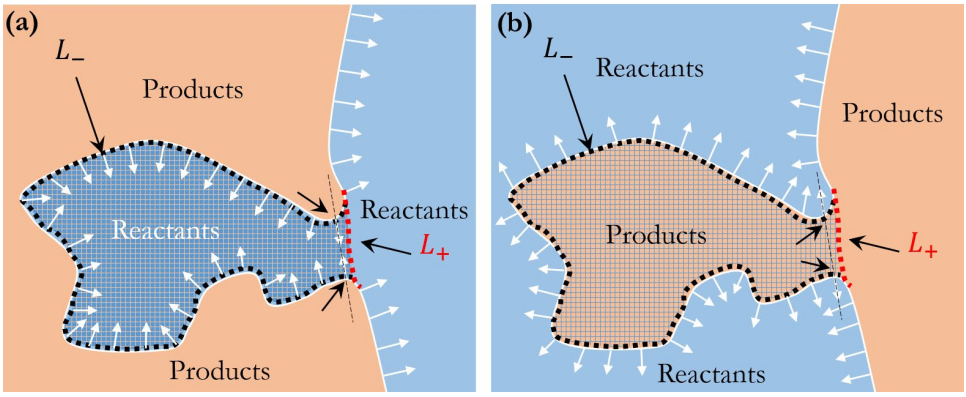

Figure 2: Schematic of examples of (a) reactant-side and (b) product-side flame-flame interactions

Distinguishing between reactant-side and product-side interactions from this technique requires appropriate processing of images obtained from image registration. Due to the closed shape of Bunsen flames, subtraction of a 'fixed' image from the registered 'moved' image results in topological differences with reactants being consumed in the middle. The length of flame edges from both 'fixed' (L_-) and registered 'moved' images (L_+) that trace the aforementioned topological differences are calculated and compared with each other. If L_- obtained from 'fixed' image is larger than L_+ obtained from the registered 'moved' image, the topological difference is registered as a reactant-side flame-flame interaction. Similarly, subtraction of the registered 'moved' image from the 'fixed' image yields with topological differences with product sides of the flame-fronts interacting. Additionally, corresponding flame edge lengths from 'fixed' and registered 'moved' images are calculated and compared, and topological differences corresponding to larger 'fixed' image flame lengths (L_-) are registered as product-side flame-flame interactions.

2.3 Uncertainty quantification in flame identification methodology

Most of the analysis relies on the adaptive threshold binarization of OH-PLIF images; here we have quantified the sensitivity of thresholding to image quality variations. The adaptive threshold binarization technique uses a threshold (C_T) based on Otsu's method in Matlab and the value of C_T changes from frame to frame. A distribution of C_T values from the time-series of binarized images can be used to calculate the standard deviation of C_T (σ_T) and this σ_T value can be used to obtain new thresholding values:

$$C_{T\_} = C_T - \sigma_T \quad \textbf{(1)}$$

$$C_{T+} = C_T + \sigma_T \quad \textbf{(2)}$$

Using these thresholding values, the flame-front edge can be traced and the total flame edge ($\mathcal{L}_f$) can be calculated. The normalized differences in the flame lengths from these new thresholds and the original thresholds can be reported as the sensitivity of the edge finding algorithm to the threshold value, $\mathcal{S}$:

$$\mathcal{S} = \left(\frac{\Delta\mathcal{L}_f}{\mathcal{L}_f}\right) \quad \textbf{(3)}$$

An example result from this sensitivity analysis are shown in Figure 3. The plots on the left of this figure report the threshold values and their deviations for three fields of view; the plots on the right column report the sensitivity of the flame length calculation to threshold value. 100 frames, every fifth frame in each data set, are chosen to calculate the sensitivity. These results for all the data sets obtained (not all shown here) show that most of the images have little variability in flame length calculations to changes in thresholding values for binarization. For most cases, the $\mathcal{S}$ value is less than 10%, indicating that variations in the thresholding values do not change the identification of the flame-front locations significantly. With low values of $\mathcal{S}$, we are confident in the method's capabilities to capture the time-varying locations of the flame-front in these flames.

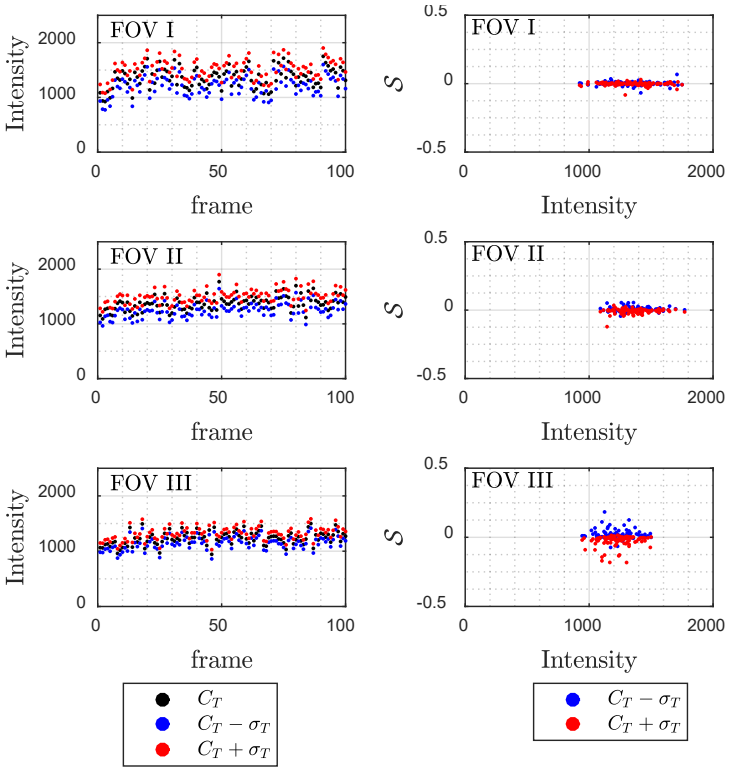

Figure 3: A-single case binarization sensitivity

Exact identification of the instant in time at which a flame-flame interaction event to occurs is limited by the sampling frequency of OH-PLIF system. For this study, the sampling time-step is 100 μs and interactions identified using the image registration algorithm occur within this time interval. The sensitivity of the image registration algorithm to the sampling rate can be studied by down-sampling the OH-PLIF data and comparing the areas of identified topological differences. A PDF plot of these areas for variation in time-steps ranging from 100-400 μs is shown in Figure 4(a). This PDF shows that as the sampling time-step increases, fewer regions of small topological differences are identified. Similarly, more regions of larger topological differences are identified. Figure 4(b) shows the variance of the areas of these regions and the plot shows that the variance of these areas also increases as the time-step is increased.

The image registration timescale must be compared to two physical timescales that represent the flame behavior we are trying to capture: a consumption timescale and a convection timescale. The consumption timescale is estimated by approximating the time required for a flame-flame annihilation event to occur and represents the time scale associated with flame extinction using the flame speed at the extinction strain rate as the appropriate velocity-scale. Time-scales associated with flame surface annihilations can be approximated using the concept of flame extinction velocity. For methane-air flames with inlet temperature of 300 K and pressure of 1 atm, the flame extinction velocity (u_{ext}) is approximately 2 m/s. From the PDF of areas in Figure 4(a), the smallest observable region has an area of 0.25 mm^2 . Assuming a filamentarity of zero for this shape, the corresponding diameter is 0.56 mm and the perimeter is 1.76 mm. Using the extinction velocity, a time-scale associated with flame surface annihilation of this circular region is: τ_{ext} = 880 μs. Therefore, a sampling time-step of 100 μs for OH-PLIF measurements in this study is able to capture small-scale annihilation events.

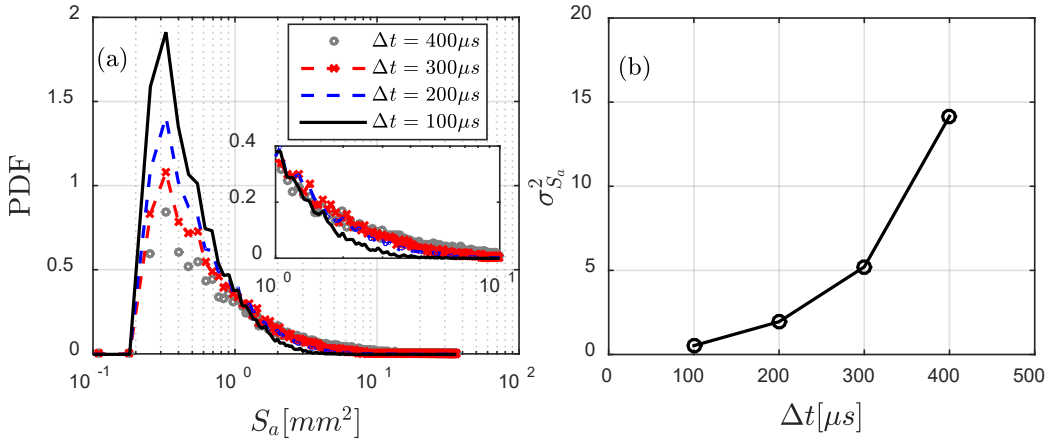

Figure 4: Sensitivity of Δt on image registration methodology for single-flame case A in FOV I: (a) PDF plot of areas of topological differences identified through image registration for different sampling rates, and (b) plot of variance of the identified areas vs. the sampling time step (Δt)

The convective timescale is driven by the mean flow velocity, which varies from 12 m/s – 28 m/s in this study. Using 12 m/s and Δt = 100 µs as a baseline, we would expect the convective timescale at 28 m/s to be approximately half of that at 12 m/s. This is effectively the same as doubling the inter-frame time, where the sensitivity of the image registration method's ability to measure topological differences in that time is given by $\sigma^2_{S_a}$ = 1.95 mm^2, as shown by Figure 4(b).

Finally, local interaction statistics in this study are quantified from two-dimensional imaging of three-dimensional turbulent flames; inferring three-dimensional flame topologies from planar measurements involves some uncertainties. In this analysis, we differentiate an actual flame interaction event from a three-dimensional flame motion that may appear like an interaction event in one plane. To understand the relative contribution from these two motions, we use the simultaneous s-PIV/OH-PLIF measurements to obtain the absolute instantaneous velocities at the centroid locations of interactions. In doing so, we assume that an interaction location with an out-of-plane velocity that is higher than the turbulent burning velocity is more likely to be a three-dimensional effect rather than a true interaction. Equation (4) is used to approximate the turbulent burning velocity for flames, where the laminar flame speed of the stoichiometric methane-air mixture is 0.4 m/s.

$$S_T = s_L \sqrt{1 + \left(\frac{u'}{s_L}\right)^2} \qquad \textbf{(4)}$$

Histograms of instantaneous out-of-plane (U_z) velocity components at the location of reactant-side interactions for dual-flames at 12 m/s bulk velocity in Figure 5. The percentage of interactions that are deemed "real" by this method is reported in each histogram, and ranges from 78-98%, with most cases being above 90%. The turbulent burning velocity used for this calculation is 2.2 m/s, which is similar to u' fluctuations in the flowfield. The location of the turbulent burning velocities are marked with a red dashed-line on the horizontal axis in each histogram. The results shown here indicate that the image registration technique can potentially be a robust methodology to identify flame-flame interactions from high-speed OH-PLIF measurements, as the fraction of the detected interactions that meet our criteria is high.

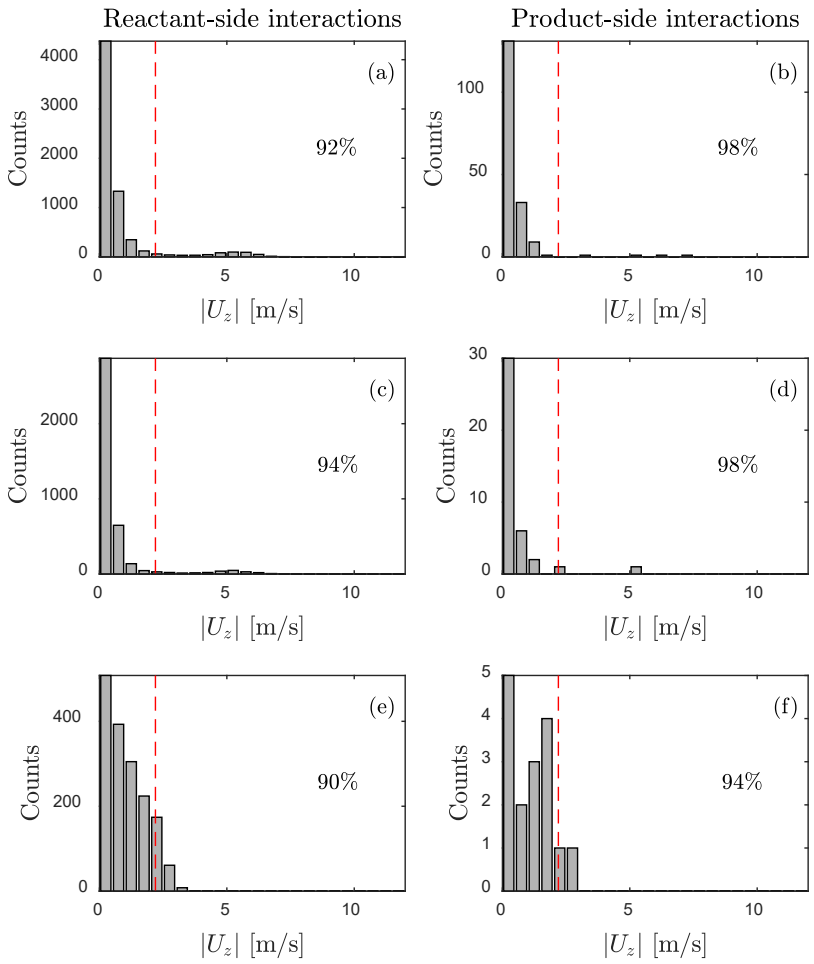

Figure 5: Histograms of the magnitudes of out-of-plane (U_z) components of instantaneous velocity at the centroid locations of interactions in dual-flames at 12 m/s bulk velocity: reactant-side interactions in (a) FOV I, (c) FOV II, and (e) FOV III; product-side interactions in (b) FOV I, (d) FOV II, and (f) FOV III

3 Flame interaction event frequency

3.1 Publications from this effort

- Tyagi, A., Boxx, I., Peluso, S., & O'Connor, J. (2019) "Statistics and topology of local flame-flame interactions in turbulent flames," *Combustion and Flame*, **203**, p. 92-104
- Tyagi, A., Boxx, I., Peluso, S., Shupp, R., O'Connor, J., (2018) "Topology of local flame-flame interaction events in turbulent flames," *Spring Technical Meeting of the Eastern States Section of the Combustion Institute*, State College, PA.
- Tyagi, A., Boxx, I., Peluso, S., Shupp, R., O'Connor, J., (2018) "Structure of flames in flame interaction zones," *AIAA SciTech*, Kissimmee, FL.

3.2 Topology of local flame interactions

Illustrations of local flame-flame interactions are shown in Figure 6 and Figure 7. In each of these figures, time series of binarized images and flame edges for local flame-flame interaction events are shown. As shown in Figure 6(a), (b) and (c), reactant-side interactions can occur in three different ways: (1) merging of local flame fronts, leading to destruction of flame surface and formation of small-scale reactant pockets, (2) merging of local flame fronts, leading only to destruction of flame surface (also known as

"cusping"), and (3) merging of flame branches in the flame tip region, leading to formation of large-scale reactant pockets (also known as "flame pinching"). In all three scenarios, flame surface destruction occurs due to flame-flame interactions ($L_- > L_+$). Additionally, cases shown in Figure 6(a) and (c) show that flame-flame interaction events could redistribute flame surface through formation of flame pockets, which typically burn out. These interaction events lead to flame surface destruction and the range of scales over which flame surface destruction occurs can change based on the topology of these events, as highlighted by these examples.

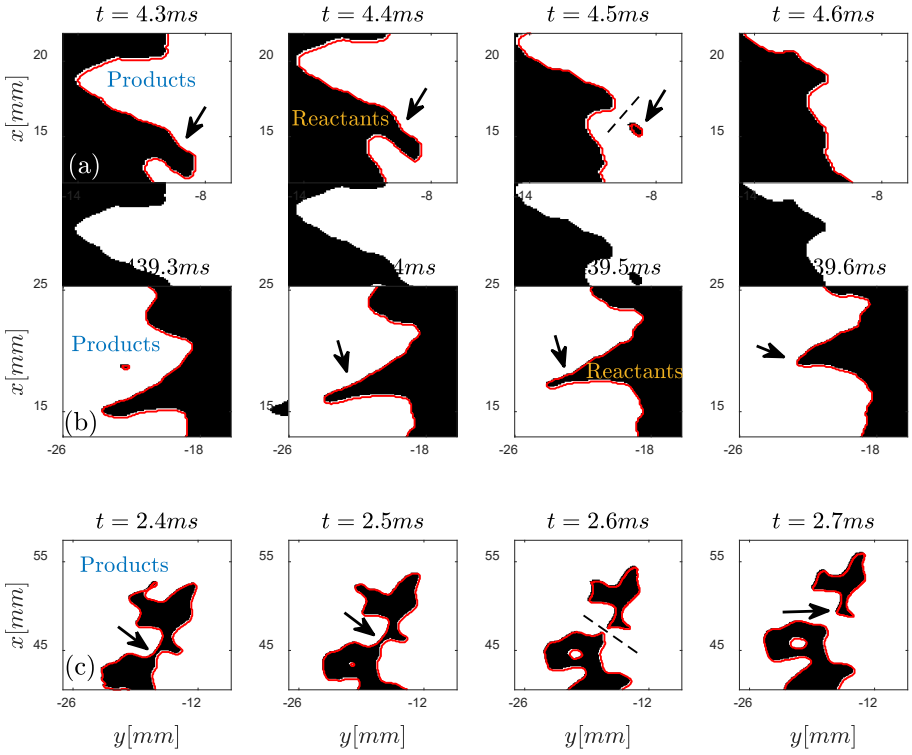

Figure 6: Time-series of a reactant-side interactions for dual-flames case A: (a) interaction leading to reactant pocket formation in FOV I, (b) interaction without pocket formation in FOV I, and (c) interaction in the flame tip region leading to formation of large-scale pockets

Figure 7 shows examples of product-side interactions of two kinds: (1) merging of the local flame front, leading to a product pocket formation, and (2) merging of the local flame front, leading to the destruction of flame surface. In Figure 7(a), the local product-sides of the flame front move toward each other, resulting in the formation of a product pocket, which convects in the free stream of reactants. However, it is unclear from planar OH-PLIF measurements whether this product region contains a reaction layer around it. Despite this ambiguity, this event highlights that product-side interactions can also change flame surface density. In contrast to this example, Figure 7(b) shows that counter-normal interactions may not necessarily lead to formation of product pockets and can sometimes result in the destruction of flame surface. Similar to the reactant-side interactions, these examples highlight that product-side interactions can occur over a range of scales.

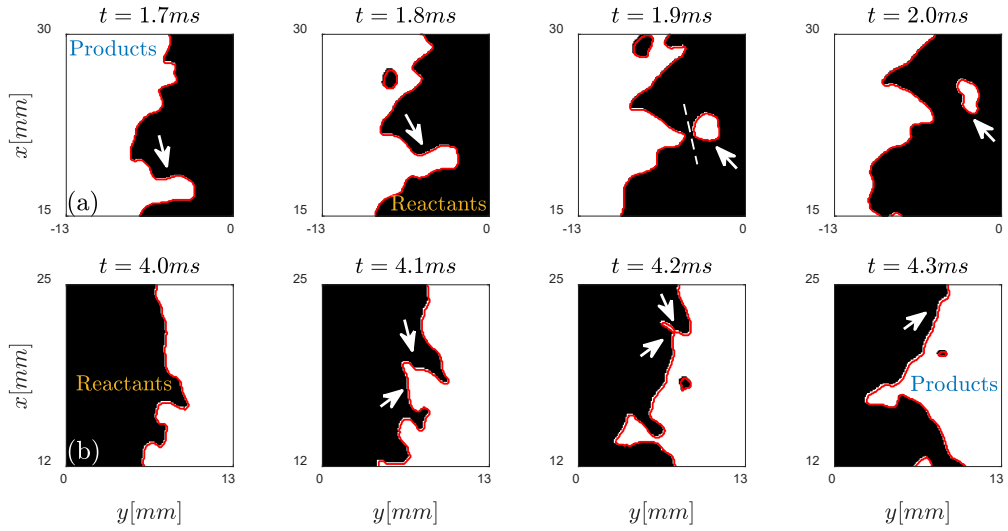

Figure 7: Time-series of a product-side interactions for single-flame case E: (a) interaction leading to reactant pocket formation in FOV I and (c) interaction without pocket formation in FOV I

3.3 Dual Bunsen burner configurations

Data has been obtained for a wide range of conditions in the Bunsen flame configuration. Table 1 shows the text matrix used in this study. The equivalence ratios for main flames and pilot flames are set to unity. For cases A-E in Table 1, the bulk velocities are varied from 12-28 m/s in increments of 4 m/s, while the flame spacing is kept constant at 30 mm (the closest spacing possible). Additionally, measurements at single-flame configurations are performed for cases A, C, and D to make direct comparisons between single- and dual-flames. For cases F-I, the bulk velocity is kept constant at 20 m/s while the flame spacing is varied from 35-50 mm in 5 mm increments. All the flames in Table 1 operate in the thin-reactions regime on the Borghi-Peters' premixed combustion regime diagram.

Table 1: Flow conditions of burners

Case	Bulk flow properties			Non-reacting inlet turbulence characteristics						S $[mm]$	Simultaneous measurements
	U $[m/s]$	Re_w	Re_h	u' $[m/s]$	L_{11} $[mm]$	λ_{Taylor} $[mm]$	$Re_{L_{11}}$	u'/s_L	L_{11}/l_f		
A-Dual	12	8500	15000	2.2	2.1	1.4	325	5.5	11.1	30	Yes
A-Single										--	No
B-Dual	16	11000	21000	2.9	2.4	1.3	484	7.2	12.5	30	No
C-Dual	20	14000	26000	3.6	2.3	1.3	575	8.9	11.8	30	Yes
C-Single										--	No
D-Dual	24	17000	31000	4.3	2.2	1.3	687	10.7	11.8	30	No
E-Dual	28	19000	36000	5	2.2	1.2	787	12.4	11.6	30	Yes
E-Single										--	No
F-Dual	20	14000	26000	3.6	2.3	1.3	575	8.9	11.8	35	No
G-Dual	20	14000	26000	3.6	2.3	1.3	575	8.9	11.8	40	Yes
H-Dual	20	14000	26000	3.6	2.3	1.3	575	8.9	11.8	45	No
I-Dual	20	14000	26000	3.6	2.3	1.3	575	8.9	11.8	50	Yes

The frequency of flame-flame interactions is defined as the number of flame surface destruction interactions identified over a duration of measurement, reported in units of interactions per milli-second. Figure 8 shows the rates of reactant-side attached flame-flame interactions for single- and dual-flame cases at a range of bulk flow velocities (cases A-E in Table 1). Figure 8(a) and (b) show the rates of reactant-side interactions ($\mathcal{R}_R[(ms)^{-1}]$) in all three FOVs. Here, the mid-point of each FOV is used to represent the downstream location and is normalized by the flame height *H*. In the dual-flame cases, the values of $\mathcal{R}_R$ for either flame show a maximum variability of ±10%; the interaction rates for dual-flames reported in Figure 8 and Figure 9 are averages of the two flames. Interaction rates increase with bulk flow velocity for both configurations. The turbulence intensity for cases A-E is approximately 18%; however, the absolute turbulence level increases as the bulk flow velocity is increased. As a result, increased wrinkling occurs in the high bulk flow velocity cases and consequently, the $\mathcal{R}_R$ values increase. Figure 10 shows the turbulence length- and velocity-scales along the $\bar{c} = 0.5$ contour as functions of downstream distance for the dual-flame cases A, C, and E. Additionally, as the bulk flow velocity increases (cases A-E), larger differences in the interaction rates are present in FOV I. For these cases, dual-flames show lower interaction rates compared with single-flames. Finally, the values of $\mathcal{R}_R$ for both single- and dual-flames generally decrease as a function of downstream distance. This decrease is a result of the change in the type of interaction with downstream distance. Further downstream, attached-flame interactions become less common and larger pocket formation events become more common.

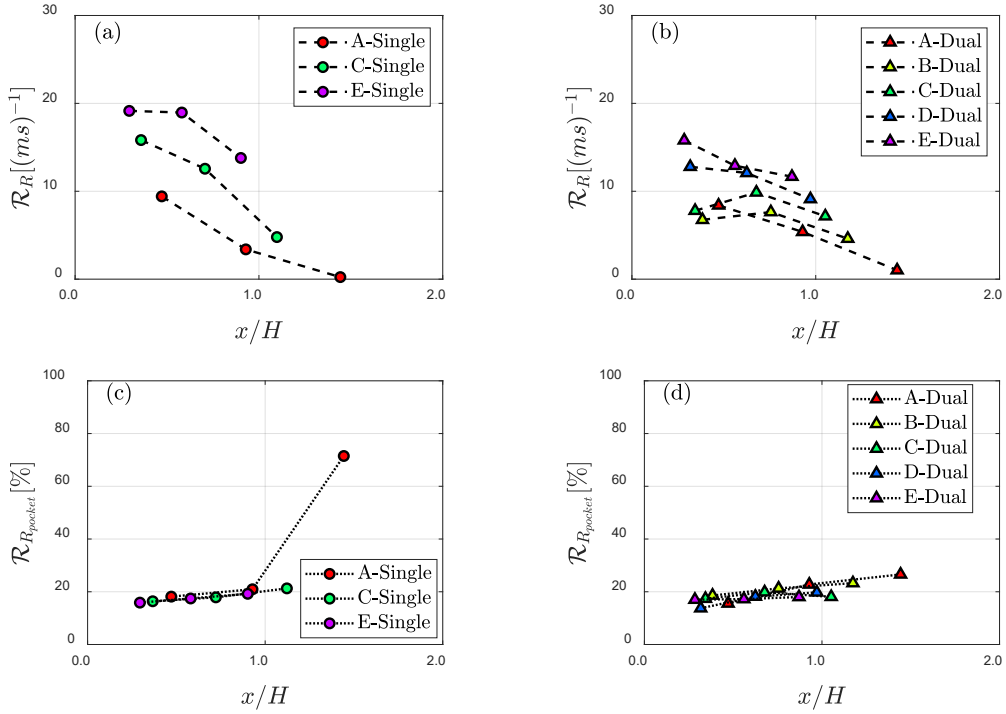

Figure 8: Reactant-side attached flame-flame interaction rates in 1/milli-second for (a) single- and (b) dual-flame configurations with variations in bulk flow velocities. Pocket formation rates in [%] from these interactions for (c) single- and (d) dual-flame configurations.

Figure 8(c) and (d) show the percentage of reactant-side interaction events that lead to pocket formation ($\mathcal{R}_{R_{pocket}}[\%]$) for cases A-E. For the single-flame cases, this percentage falls in the range of 15-22%, except for FOV III in case A. The high value (72%) for this case is attributed to the large number of flame pinch-off events. The imaging FOV in this region is not sufficiently tall to capture the motion of the flame

tip in all cases, resulting in incomplete identification of the locations of flame pinching that leads to large-scale pocket formation. This lack of information results in missing interaction events for this region, leading to the low count of attached interactions. The percentage of reactant gas pockets formed in the dual-flame cases fall in the range of 13-27%. These results show that for both flame configurations, the number of interactions leading to reactant-gas pocket formations increases as the downstream distance increases. As shown in Figure 10(a), L_{11} and L_{22} increase near the flame along the downstream direction and this increase in the turbulence scales likely increases the amount of wrinkling along the flame front. This enhanced wrinkling results in a higher probability of pocket formation rather than cusp burnout as the flame structure is highly curved. Additionally, the turbulence velocity-scales decay as a function of downstream distance near the flame, indicating that large velocity fluctuations result in more cusp burnout interactions and large integral length-scales result in more pocket-forming interactions.

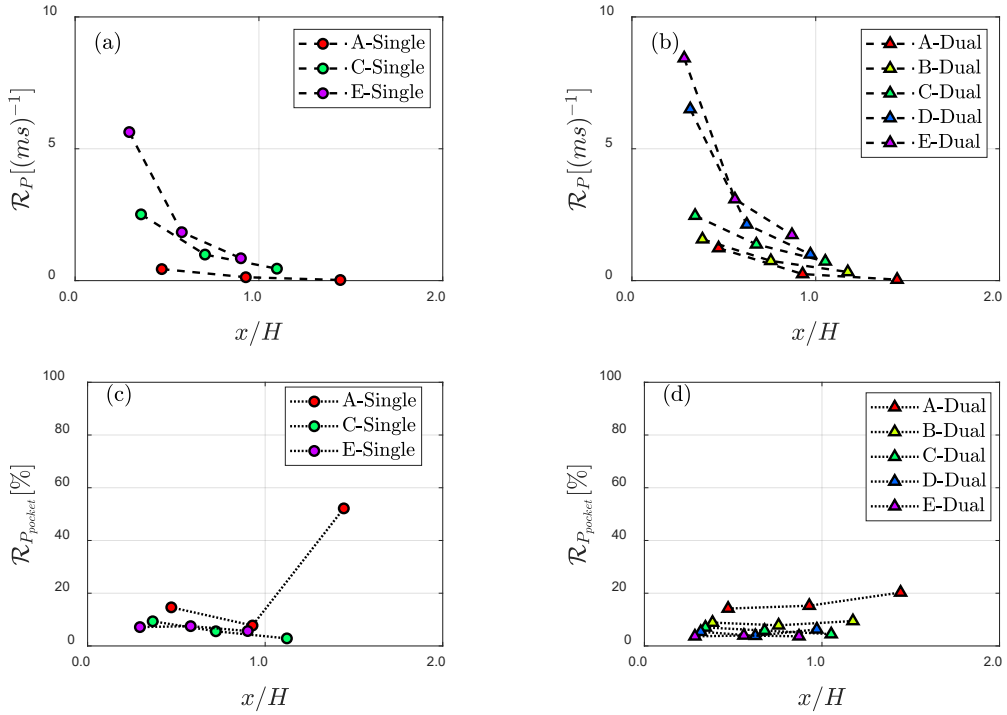

Figure 9: Product-side attached flame-flame interaction rates in 1/milli-second for (a) single- and (b) dual-flame configurations with variations in bulk flow velocities. Pocket formation rates in [%] from these interactions for (c) single- and (d) dual-flame configurations.

Figure 9 shows the rates of product-side interactions ($\mathcal{R}_P$) for the same cases as Figure 8. Like $\mathcal{R}_R$, $\mathcal{R}_P$ decreases with downstream distance and higher velocity cases lead to higher values of $\mathcal{R}_P$ for both single- and dual-flame cases. Increasing bulk flow velocity increases the local turbulence level, which allows for the possibility of local turbulence to overcome flame propagation, resulting in higher rates of product-side interactions. Additionally, larger differences are present in FOV I for all cases; these differences become smaller farther downstream as the turbulence intensity decays. Figure 9(c) and (d) show percentages of pocket formations from identified product-side interactions; these percentages are in the range of 1-15% and 3-20% for single- and dual-flames, respectively. In the case of product-side interactions, the percentage of interactions leading to formation of flame pockets decreases as the bulk flow velocity increases. This is observed for both single- and dual-flame configurations. While the increase in integral length-scales facilitates pocket-forming along the downstream direction in the case of reactant-side interactions, it does

not promote pocket formation in the case of product-side interactions. The interaction rate behaviors in Figure 8 and Figure 9 are similar for single- and dual-flame configurations. The reactant-side interaction rates are generally higher than the product-side interaction rates. However, differences exist between the absolute rate values between the two configurations. For dual-flames, $\mathcal{R}_R$ values are smaller, and $\mathcal{R}_P$ values are larger when compared with single-flames. It is likely that the presence of adjacent interacting flow fields alters the mean shear in the case of dual-flames that can change the local flow dynamics and impact the local flame-flame interaction statistics; this interaction is absent in the single-flame cases.

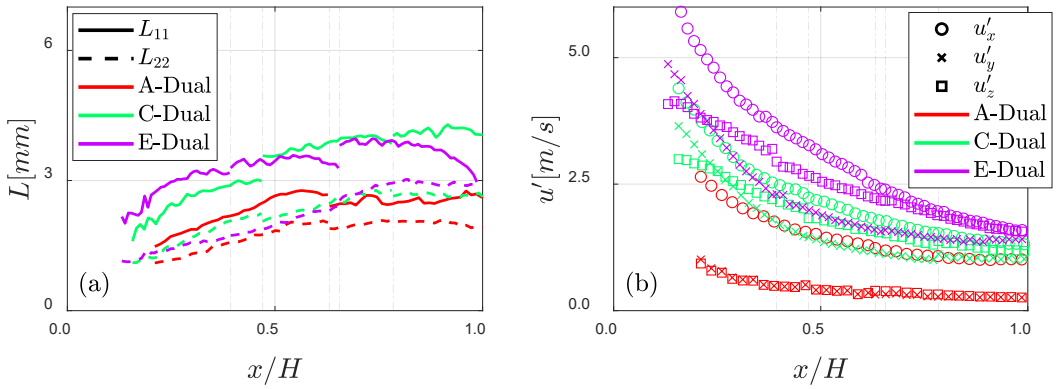

Figure 10: (a) Turbulence integral length-scales (L_{11} and L_{22}) and (b) intensities along $\bar{c}$=0.5 as functions of downstream distance for dual-flame case A, C, and E. The vertical gray-lines demarcate FOVs II and FOV III for these cases

4 Impact of flow field on flame interaction

4.1 Publications from this effort

- Tyagi, A., Boxx, I., Peluso, S., & O'Connor, J. (2019) "Statistics and topology of local flame-flame interactions in turbulent flames," *Combustion and Flame*, **203**, p. 92-104
- Tyagi, A., Boxx, I., Peluso, S., & O'Connor, J. (2018). "The role of flow interaction in flame–flame interaction events in a dual burner experiment." *Proceedings of the Combustion Institute*, **37**(2), p. 3485-2491.
- Dare, T. P., Berger, Z. P., Meehan, M., O'Connor, J. (2019). "Cluster-based reduced-order modeling to capture intermittent dynamics of interacting wakes," *AIAA Journal*, **57**(7), pg. 2819-2827
- Meehan, M., Tyagi, A., O'Connor, J., (2018) "Flow dynamics in a variable-spacing, three bluff-body flowfield," *Physics of Fluids*, **30**, pg. 025105.
- Dare, T., Berger, Z., Meehan, M., O'Connor, J., (2018) "Cluster-based reduced-order modeling to capture intermittent dynamics of interacting wakes," *AIAA SciTech*. Kissimmee, FL.

4.2 Dual-burner experiments – two flames

In turbulent flames, flame-flame interactions lead to flame area annihilation, which is an important marker for fluctuations in local burning velocity, flame stretch, and local heat release rate. Our work showed that these flame annihilation events are highly coupled to the flow field surrounding the flame interaction. Figure 11 shows the PDFs of filamentarities ($\mathcal{F}$) of reactant-side interactions for dual-flame cases A, C and E, conditioned on time-averaged progress variable ($\bar{c}$). Filamentarity ($\mathcal{F}$) is a shapefinder metric utilized to quantify topology of 2D shapes using the partial Minkowski functionals—surface area S_a and perimeter P. Equation (5) is utilized to calculate the filamentarity of attached flame-flame interactions.

$$\mathcal{F} = \frac{P^2 - 4\pi S_a}{P^2 + 4\pi S_a} \tag{5}$$

This $\bar{c}$ value for an interaction is extracted at the centroid location of the interaction shape. The PDFs of $\mathcal{F}$ conditioned on the $\bar{c}$ locations are created using a bivariate Gaussian density estimator that estimates the joint-PDFs (J-PDFs) between two independent variables. The PDFs of $\mathcal{F}$ conditioned on $\bar{c}$ show higher probabilities of reactant-side interactions occurring at $\bar{c}$ closer to 1. This observation holds true for all FOVs, as shown in Figure 11. The PDFs have a wide distribution in filamentarity and the peaks at various $\bar{c}$ values generally fall in the range of $\mathcal{F}$=0.3-0.5, indicating that the interactions typically have an elliptical shape with a major-to-minor axis ratio in the range of 4-7. Conditioned PDFs of $\mathcal{F}$ of reactant-side interactions for single-flames have very similar distributions to those shown for dual-flames in Figure 11 and are not included here. The similarity in these conditioned PDFs of $\mathcal{F}$ for single- and dual-flames shows that despite large differences in the magnitudes of $\mathcal{R}_R$between the two configurations, the interaction topologies and locations in the flame brush do not vary significantly.

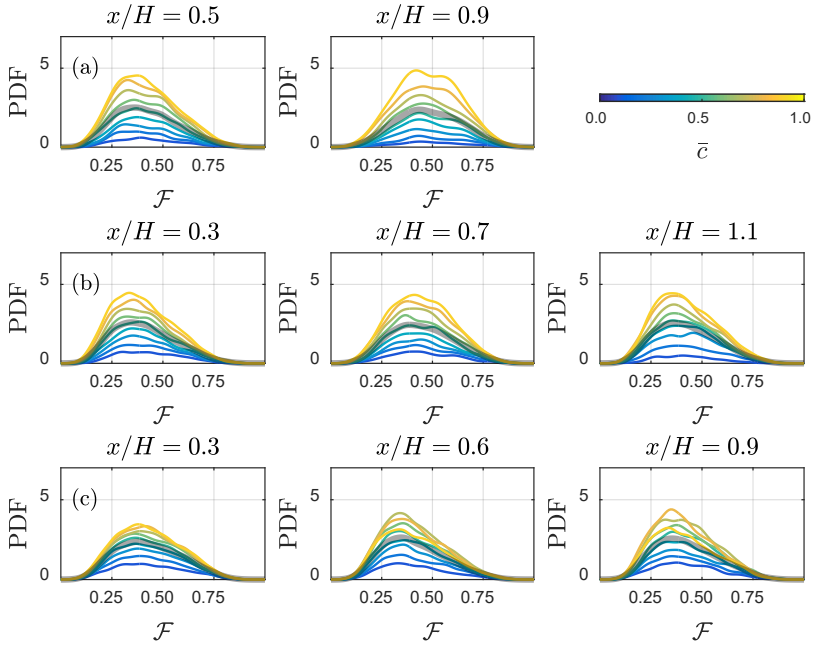

Figure 11: PDFs of $\mathcal{F}$ of reactant-side interactions conditioned on $\bar{c}$ values of 0.1-0.9 for dual-flame: (a) case A, (b) case C, and (c) case E. x/H labels represent the mid-location of each FOV. FOV III for case A does not have enough data to calculate PDFs conditioned on $\bar{c}$. Thick transparent gray lines indicate the unconditioned PDF of $\mathcal{F}$.

Figure 12 and Figure 13 show the $\bar{c}$ conditioned PDFs of $\mathcal{F}$ for product-side interactions of single- and dual-flames. In both configurations, higher probabilities of product-side interactions exist at $\bar{c}$ closer to 0 in FOV I. The conditioned PDFs show a wide distribution for $\mathcal{F}$, showing that product-side interactions can also occur at a range of shapes. These conditional PDFs peak for a range of $\mathcal{F}$ =0.3-0.5 for both single- and dual-flames in FOV I. Although values of $\mathcal{R}_P$ can be different between single- and dual-flames, their morphology remains similar in the FOV I between the two configurations, likely because of weak interaction between the flowfields. There are significant differences in the most probable $\mathcal{F}$ value at various $\bar{c}$ in FOV II. For single-flame cases A and C, higher $\bar{c}$ values ($\bar{c}$>0.3) show higher probabilities compared with lower $\bar{c}$ values, indicating that higher probabilities of product-side interactions shift location in the

flame brush. Additionally, the peaks of the PDFs shift toward higher values of filamentarity ($\mathcal{F} \geq 0.5$) in single-flame case A, implying the occurrence of unidirectional stretching of the product-side interaction topologies. PDF plots for single-flame case E in FOV II follow those from FOV I and peak at similar values of $\mathcal{F}$. In FOV II, the distribution of interactions is somewhat evenly spread in $\bar{c}$ space for dual-flames case A. The probabilities still show a peak in the range of $\mathcal{F}$=0.3-0.5; however, the distribution becomes wide. PDF distributions in FOV II remain similar to FOV I in the case of dual-flames C and E. Finally, comparisons in FOV III between single- and dual-flames case C show that for the single-flame configuration, the maximum probability occurs for $\bar{c}$~0.6, whereas in the dual-flame configuration, maximum probabilities still occur near the reactant-side of the flame brush in the range of $\bar{c}$=0.3-0.4. For both configurations of case E, the PDF plots in FOV III show that most interactions are still occurring near the reactant-side of the flame brush, with peaks for $\mathcal{F}$=0.3-0.5. These PDF plots suggest that most of the interactions occur in the $\bar{c}$ ranges of 0.3-0.5 for these flames. The $\bar{c}$ conditioned plots of u' near the flame-front in Figure 10 show that the mean value plots of u' components in $\bar{c}$ space coincide with the plots of u' conditioned in the range of $0.3 \leq \bar{c} \leq 0.5$. The overlap of the mean and the conditioned u' plots suggests that velocity fluctuations at these $\bar{c}$ values are driving the large probabilities of flame-flame interactions identified for these flames.

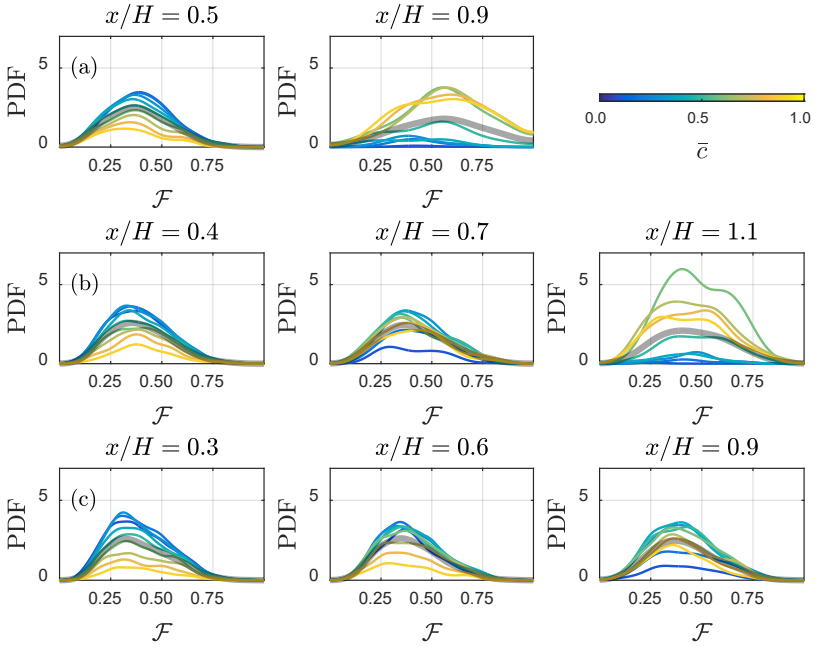

Figure 12: PDFs of $\mathcal{F}$ of product-side interactions conditioned on $\bar{c}$ values of 0.1-0.9 for single-flame: (a) case A, (b) case C, and (c) case E. x/H labels represent the mid-location of each FOV. FOV III for case A does not have enough data to calculate PDFs conditioned on $\bar{c}$. Thick transparent gray lines indicate the unconditioned PDF of $\mathcal{F}$. The color bar represents values of $\bar{c}$

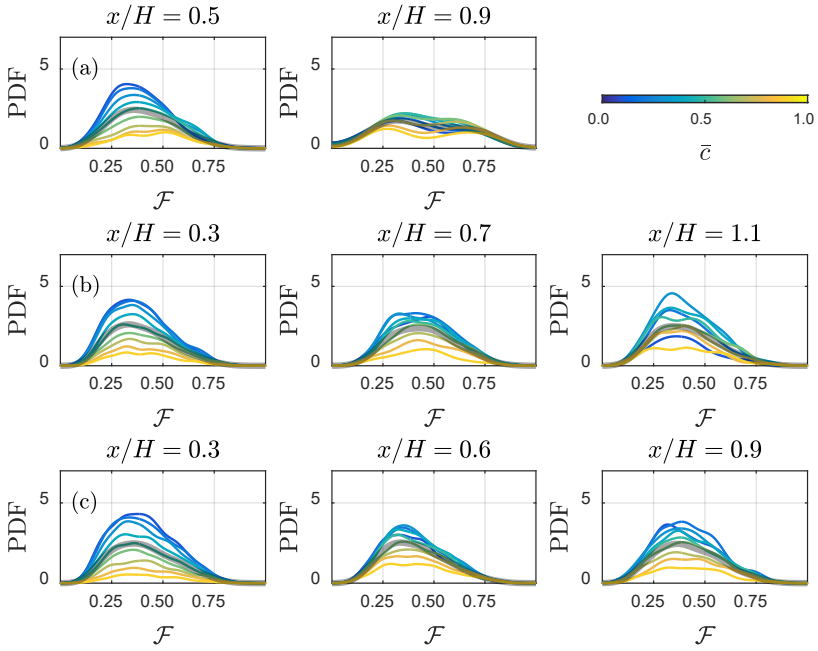

Figure 13: PDFs of $\mathcal{F}$ of product-side interactions conditioned on $\bar{c}$ values of 0.1-0.9 for dual-flame: (a) case A, (b) case C, and (c) case E. x/H labels represent the mid-location of each FOV. FOV III for case A does not have enough data to calculate PDFs conditioned on $\bar{c}$. Thick transparent gray lines indicate the unconditioned PDF of $\mathcal{F}$. The color bar represents values of $\bar{c}$

The $\mathcal{F}$ distributions shown above illustrate the shapes of flame-flame interactions and flame wrinkling due to local turbulence and flame propagation. The morphology of these interactions identified through $\mathcal{F}$ distributions not only include the wrinkling of the consumed flame surface but also the remaining flame surface. Since the flame is affected by local turbulence, a simplified approach to quantify the effect of turbulence on the morphology of interactions is to approximate the shape of the interaction as an ellipse and calculate its major-to-minor axis ratio. In doing so, the normalized second central moments of the region are matched with an ideal ellipse and the major and minor axes are extracted. The ratio of these axes can then be compared to the anisotropy of the turbulence length-scales (L_{11}/L_{22}) near the flame. The interaction shape axis ratio values obtained from this method fall in the range of 1.5-2.0 and the values of L_{11}/L_{22} peak near 1.5-1.8 for various downstream locations. Turbulent eddies with this oblong shape can affect the morphology of the flame structure and likely impact the shape of flame-flame interactions. However, this may be a coincidence, as many of the destroyed area shapes are not truly elliptical. Instead, we can consider the local orientation of these interactions to the principal orientations of the local strain rates to understand the link between the local flow field and flame-flame interactions.

The shapes of flame-flame interactions cannot be assumed as ellipses. However, fitting ellipses can be used to approximate the orientation of these irregular shapes. Major axes of the fitted ellipses are identified to find the local angles (θ_b) formed between these axes and the Cartesian y-axis, as shown in Figure 14 (a). To assess the alignment of the interaction shape with the local flow field, the orientation of the fluid near the interaction event can be calculated using its velocity gradients. The principal angle θ_p is the orientation of the principal plane where the shear component of strain rates is zero. Calculating this principal plane allows for calculating the orientation of the most extensive and the most compressive fluid strain rates. In the context of the flame-flame interaction shape orientation, the alignment between θ_b and θ_p can show the directions of pure compression and extension of the local fluid element as the flame-flame interaction

occurs. Both θ_p and θ_b are measured in [0º, +180º] and the differences between these angles are reported as $\Delta\theta$. Cosines of $\Delta\theta$ quantify the alignment between θ_b and θ_p and fall in [0, +1], with perfect alignment at +1, and no alignment at 0.

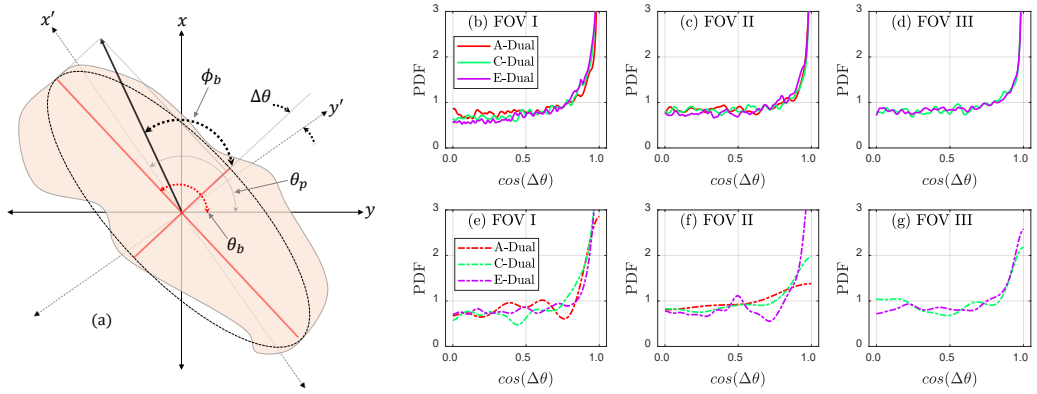

Figure 14: (a) Schematic of the orientation of flame interaction shape, principal plane of strain rates with respect to the Cartesian coordinate frame. Comparison of PDFs of the alignment between the major axis of the flame-flame interaction shape (θ_b) and the principal angles of the strain rates (θ_p). Reactant-side interaction statistics are shown in (b) FOV I, (c) FOV II, and (d) FOV III; product-side interaction statistics are shown in (e) FOV I, (f) FOV II, and (g) FOV III

Figure 14 (b)-(g) shows the PDFs of cosines of $\Delta\theta$ for dual-flame cases A, C, and E in all three FOVs. Plots for both reactant- and product-side interactions show that for all three cases, most of these interactions are aligned with the principal planes. These PDF plots show that the most probable value of the cosine of $\Delta\theta$ is +1, indicating that the directions of the most extensive and the most compressive strain rates align with the directions of the major and minor axes of the flame-flame interaction shapes, implying that compressive forces in the local flow field lead to the merging or pinch-off of the flame-fronts for these flame-flame interactions.

4.3 Dual-burner experiments – one flame, one flow

A dual burner experiment is used to investigate how flow interactions affect local flame-flame interaction in turbulent premixed flames. The presence of adjacent flows influences the local structure of these flames and understanding the sensitivity of these flames to adjacent flows is essential for multi-nozzle combustion devices. To study this sensitivity, a high-aspect-ratio Bunsen flame operating at a constant flow velocity is placed adjacent to an identical burner with non-reacting flow at varying velocities. High-speed OH-planar laser induced fluorescence and stereoscopic-particle image velocimetry measurements are performed to capture flame-front locations and velocity fields. A non-rigid image registration technique is used to calculate the local flame-area variations that occur due to topological differences, and conditional statistics are extracted to relate the local behavior to changes observed in the global behavior of the flames. Extracted flame curvatures and time-averaged progress variables conditioned on flame-flame interactions show differences existing in the inner and outer flame branches near the flame-attachment region. Statistics of these results were collected and compared for all test cases.

The experimental facility consists of two identical, premixed high-aspect-ratio Bunsen burners with 100 mm x 10 mm exit planes (Figure 15). Each burner has a lower and an upper section, measuring 178 mm and 160 mm tall, respectively. The lower section contains the inlet for the premixed reactants (natural

gas and air), and a ceramic honeycomb flow-straightener. The upper section contains an additional ceramic honeycomb flow straightener and two perforated plate turbulence generators. These plates have 3.175 mm hole-diameters, 40% open area, and are mounted 30 and 10 mm upstream of the burner exit. The plates are designed to produce a uniform flow with high turbulence at the burner exit. Each burner also contains two pilots, thin pilot flames aligned with the 100 mm edges of the burner exit that anchor the flame and a wider outer pilot that back-support the flames downstream.

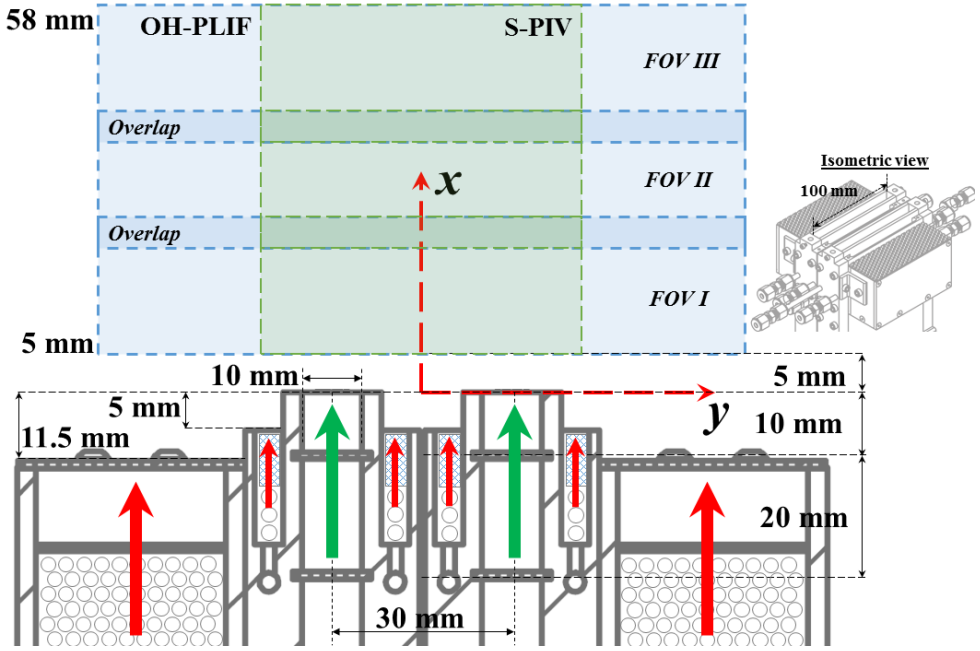

Figure 15: Burner cross-section: larger green arrows represent the main flame flow passage, smaller red arrows and larger red arrows represent the pilot flame flow passage.

This versatile facility can be operated in a variety of modes. In this study, a *flame-flow* configuration is used, where one burner supports a flame and the other flows air at varying velocities. This flame-flow configuration allows us to change the flow interaction between neighboring burners while maintaining a stable flame in the reacting burner. Using this configuration, flames can be subjected to significant flow interaction on one side, while the other flame branch experiences quiescent conditions. This allows for studying flame-flow interaction effects on the inner branch of the left-burner flame and keeping the boundary conditions on the outer branch of the flame similar to most canonical single burner experiments. Table 2 shows the test matrix for this study. In this table, U_{Left} and U_{Right} correspond to the bulk flow velocities of the reacting- and non-reacting burner, respectively. For all cases in Table 2, the premixed reactants are natural gas and air for main and pilot flames and all the equivalence ratios are kept constant at unity. Additionally, the bulk flow velocities of the thin pilot flames and the outer pilot flames are kept constant at 3 m/s and 4.3 m/s, respectively. The center-to-center distance (S) between the burners is 30 mm. For each case, the integral length and velocity scales measured at the reacting burner exit are 2.1 mm and 2.2 m/s, and the corresponding turbulent Reynolds number is 328. The turbulent kinetic energy measured at this location is 4.4 m^2/s^2.

Table 2: Test matrix for all flames studied for flame-flow interaction

Case	U_{Left} *[m/s]*	U_{Right} *[m/s]*
A	*12*	*20*
B	*12*	*25*
C	*12*	*30*
D	*12*	*35*
E	*12*	*40*

Figure 16 shows the time-averaged vorticity along the inner and outer shear layers of the burner at non-reacting conditions. The locations of mean shear were obtained by identifying the maximum absolute value of the mean vorticity as a function of downstream distance for the inner and outer shear layers, individually. The vorticity is calculated in the first two FOV, where the dotted gray lines indicate the overlap region between the laser sheets. The time-averaged vorticity differs between the inner and outer shear layers at the burner exit; however, as the vorticity decays with downstream distance, the vorticity in the inner and outer shear layers become similar. These vorticity results, as well as other analyses of the flow field, indicate that the structure of flow field differs on either side of the flame near the flame attachment point. As the flow develops downstream, the shear layers merge and the vorticity and turbulence intensity (not shown) become more uniform across the span of the burner.

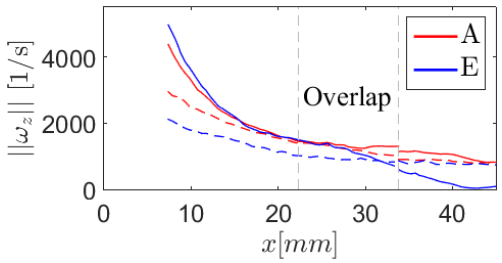

Figure 16: Mean vorticity along the inner-(solid) and outer-mean shear locations (dashed) for the left burner.

The presence of the jet on one side of the flame affects the time-averaged progress variable field ($\bar{c}$). The time-averaged progress variable is calculated by averaging binarized instantaneous images of reactants (c=0) and products (c=1). Figure 17 shows two examples of $\bar{c}$ images for flames A and E. The progress variable fields show the flame leaning towards the centerline of the two burners; the bias is greater for flame E than flame A. Horizontal slices of $\bar{c}$ in Figure 17 at various streamwise locations show this bias more concretely. In this figure, the vertical-dashed line represents the centerline of the reacting burner. The distribution of $\bar{c}$ near the nozzle exit is symmetric with respect to the burner centerline. However, $\bar{c}$ distributions further downstream show that the time-averaged flame structure bends towards the centerline of the experiment as a result of enhanced entrainment by the non-reacting burner. The $\bar{c}$ distribution biases further towards the centerline as the non-reacting jet velocity increases, as a result of increased entrainment. These results imply that in a multi-nozzle facility, such as the current experiment, statistics that are conditioned on $\bar{c}$ are dependent on adjacent flow conditions, and canonical single-burner experiment cannot accurately capture these effects.

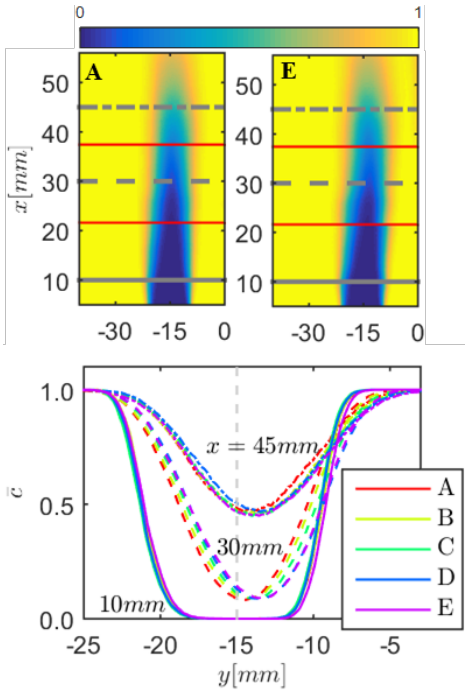

Figure 17: Stitched progress variables and horizontal slices at various downstream locations. Red lines represent the stitched locations.

The flow interaction also has an impact on the local characteristics of the flame, including the flame curvature statistics and the frequency and topology of flame interaction events. Figure 18 shows the curvature PDFs for the inner and outer branches of all flames. These PDFs show that the inner branch has more negative curvatures than the outer branch in all cases. The PDF trends in FOV I indicate that a large number of curvatures are negative, illustrating that the inner-flame branches are more negatively curved than the outer-flame in these flames, which can lead to more reactant-side interactions.

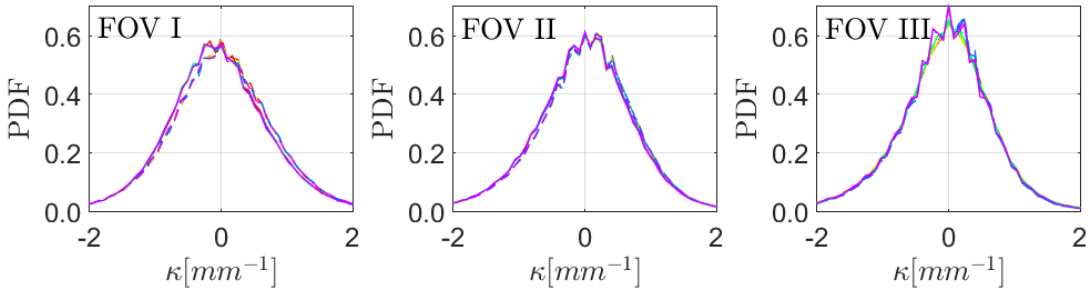

Figure 18: PDF of flame front curvatures for outer-(dashed) and inner-branches (solid) of the left burner flame.

The negative bias in the flame-front curvatures is only observed in the first FOV. Turbulence development further downstream seems to equalize the curvature statistics between the inner and outer flame fronts. The bias of negative curvatures in FOV I is indicative of differences in the shear layer development between the inner and outer shear layers, which affect the flame attachment regions. The similarity of curvature PDFs between the inner and outer branches in FOVs II and III likely reflects the development of the inner and outer shear layers. Additionally, the velocity of the non-reacting jet adjacent

to the slot flame does not affect the flame curvature PDFs. These differences in flame curvature PDFs near the flame attachment region have implications for interacting flow fields in multi-nozzle devices. In particular, the flow-interaction effects seem limited to the flame base, whereas the turbulent flow development downstream washes out the effects of flow interaction. This result means that single-nozzle geometries may capture the behavior of flames at further downstream distances, but possibly not near the flame-attachment region.

Changes in the curvature PDFs indicate that the instantaneous topology of the flame is different on the inner and outer branches, and one reason may be differences in local flame interaction. Flame interaction events are identified using a non-rigid image registration technique, which compares a pair of high-speed OH-PLIF images to map the transformations in the flame front due to local convection of the flame. The centroids of these regions are calculated to identify the location of each interaction. Figure 19 (bottom) shows examples of identified interactions with black markers representing the centroids of these interaction regions. The centroids are used to identify the location of interaction events and time-averaged progress variables extracted at the centroid locations are called flame interaction conditioned progress variables. Curvatures are extracted from 'fixed' flame edge pixels that are nearest to flame interaction centroids and are called flame interaction conditioned curvatures. These curvature values give a general sense of wrinkling of the flame before the occurrence of an interaction event.

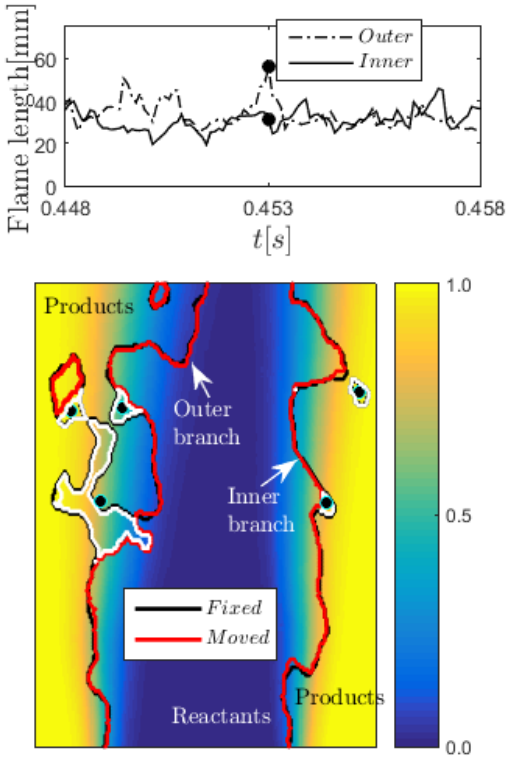

Figure 19: Instantaneous flame branch lengths (top) and flame edges and flame-flame interactions (bottom) for case E.

Figure 20 shows the number of flame-flame interactions occurring in the inner and outer branches of the flames. In FOV I, the number of interactions in the inner branch is smaller than in the outer branch; this finding aligns with the curvature PDF results, where the inner branch displays more negative curvatures. In FOV II, the differences are smaller, which is reflected in the curvature PDF results as well. In FOV III, the number of interactions occurring in the inner and outer branches are similar, likely due to shear layer

merging and the proximity of the two branches at the tip. Analysis of the flame edge movies shows that a majority of interactions occurring in FOV III are pocket formations. For flame E, the number of interactions is quite large as compared with the rest of the test cases. The flame-edge movie for this case shows that large numbers of pockets are formed in this region, and some pockets break into several smaller pockets that eventually burn out. The enhanced interactions in FOV III of flame E are likely driven by the interaction with the high-velocity jet adjacent to the flame, which entrains the tip of the flame at these high speeds.

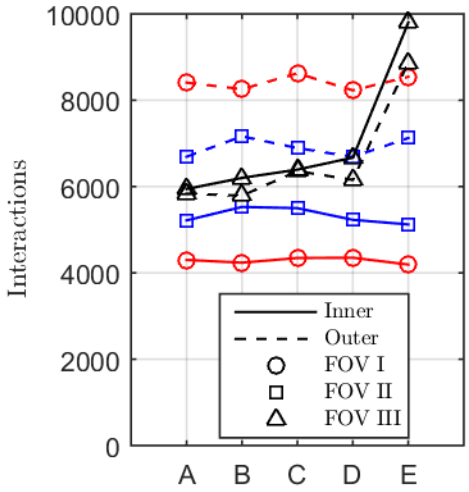

Figure 20: Number of flame-flame interaction events on the inner- and outer-branches of the left burner flame.

Using the centroid of the flame-flame interactions, flame curvatures and time-averaged progress variables can be conditionally extracted to identify topological features of the interaction sites. Figure 21(a) and (b) show the PDFs of these conditional flame curvatures and $\bar{c}$, respectively. The curvature PDF shows that the inner branch interactions tend to have more negative curvatures than the outer branch interactions. The mean interaction conditioned curvatures for the outer flame branch are more positive than that for the inner flame branch, which are consistent with the observations in Figure 21(a). Figure 21(b) shows the PDF of the conditional $\bar{c}$ values at the locations of flame-flame interactions. This PDF shows the impact of entrainment of the flame by the adjacent jet; a high number of interactions occur in $\bar{c}$=0.9-1 locations for the inner flame branch but not for the outer. This entrainment of the flame is also evident in Figure 17, where the minima in $\bar{c}$ shift away from the centerline of left burner. The differences between the inner and outer branches in the conditional $\bar{c}$ PDF suggest that conditional statistics can significantly vary in the near-fields of interacting versus non-interacting flames.

Inspection of flame-edge movies shows that the size of the interaction events are different in the inner and outer branches. The inner branch interactions, on the whole, have smaller length scales as compared to the outer branch interactions. Figure 19 shows an example of an instantaneous interaction occurring in both the inner and outer branches of the flame. In the bottom part of this figure, the white edges represent the flame-front reduction regions in a time step Δt from the image registration technique. The red edge (fixed) represents the flame at the first time and the black edge (moved) represents the flame at the next time step. A time series of the inner and outer flame-branch lengths for this FOV is also shown in the top part of this figure, where black dots on each flame-branch length time series represent the time instant of the flame edges shown in bottom part of the same figure. The flame-branch lengths for each branch are calculated by summing the arc length of the instantaneous flame-branch edge, including pockets. Large length-scale

interactions on the outer branch have a bigger impact on the global flame length, or in a three-dimensional sense, the flame area. The inner branch, on the other hand, experiences small length-scale interactions, and hence, the global flame length variations are usually smaller. Significant reactant pocket formation and consumption is also observed due to the large length-scale interactions in the outer branch. From our observations of the instantaneous velocity fields, it is likely that large-scale vortices are driving these large length scale interactions in the outer branch of the flames. The large-scale interactions illustrate the importance of understanding large-scale fluid motions and the impact that flow interaction has on the hydrodynamic stability characteristics of the flow and flame behavior.

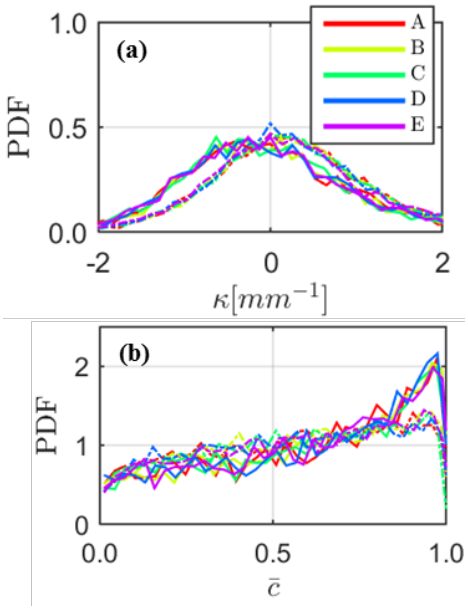

Figure 21: (a) PDF of flame interaction conditioned curvatures, (b) PDF of flame interaction conditioned ($\bar{c}$) in FOV I for the inner- (solid) and outer- branches (dashed).

5 Impact of flame shape on flame interaction

5.1 Publications from this effort

- Tyagi, A., Boxx, I., Peluso, S., & O'Connor, J. (2019) "Statistics of local flame-flame interactions in flame interaction zones of two V-flames," *AIAA SciTech Forum*, San Diego, CA.

5.2 Interaction of adjacent V-flames

The flame structure and dynamics of interacting turbulent premixed flames are dependent on interactions between the flow fields and scalar fields of individual flames. Studies have shown that local flame-flame interactions introduce a variety of effects on flame structure and propagation by changing the statistics of flame curvature, displacement speed, flame area fluctuations, and stretch-rates. The topology of interaction events can vary significantly in the interaction zones of turbulent flames. These interactions can also result in the formation of unburned and burned gas pockets. Understanding the behavior of these interaction events is of important to capture the destruction of the flame surface to develop better sub-grid scale turbulent combustion models for enhancing the design and operation of modern combustion devices. The goal of this study is to characterize the behavior of two interacting V-flames and the local flame-flame interaction characteristics in their interaction zones. High-speed OH-planar laser-induced fluorescence (OH-PLIF) is implemented to obtain instantaneous flame front locations of rod-stabilized V-flames in a dual-burner experiment. A non-rigid image registration technique is applied to flame images to track the

topological changes occurring in small time steps. In particular, results are presented for the dynamics of the interaction zones of these flames to illustrate that large-scale oscillations are important in the occurrence of small-scale flame-flame interactions. Lower arrival frequencies for flame-flame interactions are widely distributed along the streamwise direction, connecting the large-scale global behavior to the sub-grid level behavior of turbulent V-flames.

Table 3 shows the operating conditions for V-flames investigated in this study. For these flames, the equivalence ratio (ϕ) is kept close to 0.9 and the flame spacing (S) is kept at 55 mm to ensure stabilization of flames on the bluff-bodies in each burner. While the equivalence ratio varies slightly, we do not expect it to significantly alter the flame interaction behavior because the flame speed and stretch sensitivity of the flames in this range are not highly sensitive to small changes in equivalence ratio.

Table 3: Operating conditions for flames studied in the paper

Case	U $[m/s]$	ϕ	u' $[m/s]$	L_{11} $[mm]$	u'/s_L	L_{11} $/l_f$	$Re_{L_{11}}$	S $[mm]$	FOV
Flame A	13	0.90	2.3		6.4	8.6	343		
Flame B	18	0.93	3.2	2.2	8.9	9.2	500	55	IV
Flame C	19	0.95	3.4		9.4	9.6	555		

Figure 22(a) shows the time-averaged progress variable ($\bar{c}$) fields of flames A - C in the interaction region. Results from this region are particularly interesting as the merging of flow fields from both burners can be expected in this region and a large amount of wrinkling is present along the flame fronts. Visually, $\bar{c}$ fields show minor differences in flame development between the left and the right burners. These may exist due to minor geometry differences in the turbulence generation plates between the left and the right burner and it is believed that this difference has negligible effects on the analysis carried out in this study. The $\bar{c}$ fields between flames A - C show little variation between each case, indicating that small variations in turbulence levels do not significantly affect the time-averaged flame structure. To highlight the differences in flame structure in the central region, horizontal slice comparisons of $\bar{c}$ of flames A - C at various downstream locations are shown in Figure 22(b). The $\bar{c}$ profiles for these flames show values greater than zero in this region, indicating that flame fronts along the inner flame branches interact with each other. These inner branches of the left and right flames do not mutually merge with each other in this region; however, strong flame front motions are present in the cross-stream directions along the inner flame branches, indicating that the presence of an adjacent flame results in changes in flame propagation, as highlighted by the $\bar{c}$ contour lines in Figure 22(a). While the outer flame branches have densely packed $\bar{c}$ contours, the inner flame branches show sparse distributions of some of these $\bar{c}$ contours. Additionally, $\bar{c}$ = 0.1 - 0.3 contours for the inner branches of left flames are found to be connected to those of the inner branches of the right flames. This indicates that the inner flame fronts can be frequently found near the centerline of the experiment. For this study, we call this central region as the interaction zones of these flames.

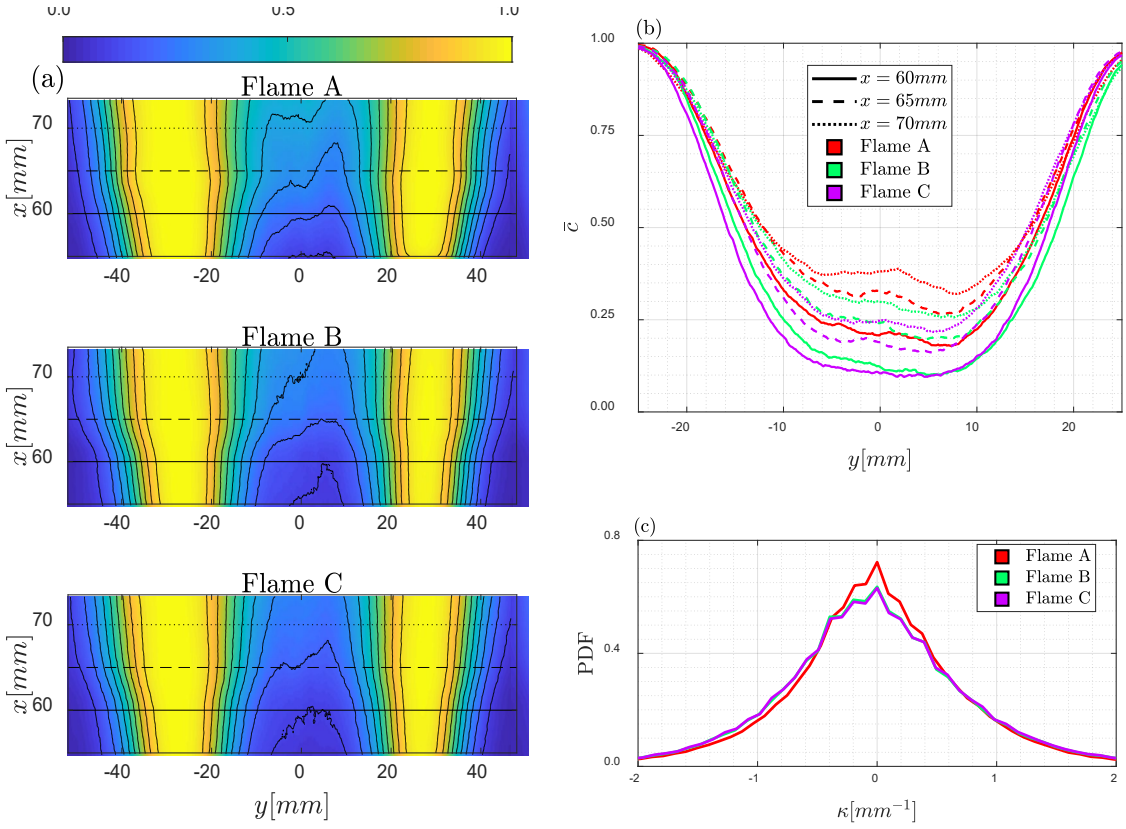

Figure 22: (a) Time-averaged progress variable fields ($\bar{c}$) for flames A - C in FOV IV, (b) horizontal slice comparisons of $\bar{c}$ at x = 60 mm, 65 mm, and 75 mm, and (c) PDFs of total flame curvatures (κ)

Comparisons between the inner and outer flame branches for all cases show that differences in spatial distributions exist for $\bar{c}$ = 0.1 - 0.5. Larger differences exist between adjacent $\bar{c}$ contours in this range in the inner flame branches compared with the outer flame branches. For example, the spatial variation between $\bar{c}$ = 0.1 and $\bar{c}$ = 0.5 in the inner branch of the left flame for flame C is as large as 18.4 mm, while the same $\bar{c}$ spatial variation in the right branch is 7.7 mm, showing that the inner flame front spatial variation is at least two times as large as the outer flame front. These differences suggest that large-scale fluctuations along the flame front in the cross-stream direction are present in the inner flame branches that may exist due to interactions between the two flames. For flame A, $\bar{c}$ values vary from 0.2 - 0.4 vertically along x = 60 mm - 70 mm. However, for flames B and C, $\bar{c}$ values vary from 0.1 - 0.3 and 0.10 - 0.25, respectively. Less variation in $\bar{c}$ values for flames with higher bulk flow velocities shows that increasing Reynolds number results in a lower probability of finding the flame front in the interaction zone. These differences suggest that interacting flames affect the distribution of the flame brush in the interaction zone and while the interaction only affects a small range of the flame brush ($\bar{c}$ = 0.1 - 0.5), it can also affect the dynamics of the flame structure in this region. As noted previously, the local flame structure directly correlates with the local turbulent burning velocity and in the next few sections, the behavior of the local flame structure is characterized by presenting statistics of the local flame-flame interaction dynamics of these flames.

Flame-flame interactions can occur in two ways: normal or counter-normal. For this study, normal interactions are called '*reactant-side interactions*' and counter-normal interactions are called '*product-side interactions*.' Examples of these interactions for flame C are shown in Figure 23, where instances of

reactant-side interactions are shown by blue arrows and instances of product-side interactions are shown in green arrows. Both types of interactions can result in annihilation of flame surface and formation of flame pockets. In reactant-side interactions, the flame surface can either fold on itself and create a pocket of reactants that is consumed, or mutual interaction can occur between two sections of the flame, resulting in destruction of the flame surface. Like reactant-side interactions, product-side interactions can also either result in pure annihilation of the flame surface or form flame pockets of combustion products. Figure 22(c) shows the PDFs of total flame curvatures of these flames in FOV IV. These curvature PDFs show that a large amount of wrinkling is present along the flame front, suggesting that frequent flame folding and pinch-off events that lead to flame-flame interactions can occur in this FOV, affecting the local turbulent burning velocity of the flames. These flame-flame interaction events are typically three-dimensional and using by two-dimensional imaging, only the in-plane component of these events can be identified and reported in this study.

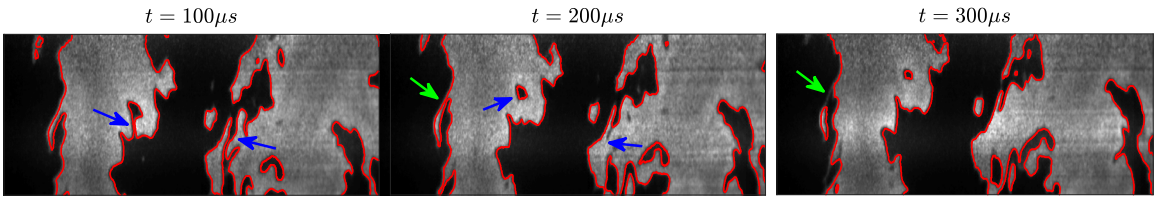

Figure 23: Reactant-side and product-side flame-flame interactions for Flame C

Using the image registration methodology, statistical quantification of reactant- and product-side interactions is performed. Figure 24(a) shows the rates of reactant- and product-side interactions ($\mathcal{R}_{Int}$) in Hertz for flames A - C for a period of one second. Since the merging of an existing flame pocket with a flame front is not counted as an interaction in this technique, these rates only include interaction events that occur due to pinch-off or folding of the attached flame front. These results show that more flame-flame interactions events occur as the turbulence levels are increased. Increasing the turbulence levels increases the range of scales of wrinkling on the flame and leads to interactions occurring at a wider range of scales. This observation is true for both reactant-side and product-side interaction events. However, a direct comparison between the two types of interaction rates shows that reactant-side interactions occur almost twice as often as product-side interactions in all flames. In the case of reactant-side interactions, the flame fronts propagate towards each other locally while consuming the reactants, showing that flame dynamics are dominant by such events. For product-side interactions to occur, the local flow needs to be highly strained to counter flame propagation in order to cause the flame fronts to fold and merge on the product-side. The vast differences in the reactant- and product-side interaction rates suggest that flame propagation is dominant over the flow strain effects for a majority of the flame-flame interaction events in these flames.

Due to the amount of wrinkling present in flames in this FOV, a large number of flame pockets appear in the OH-PLIF plane of measurement. These flame pockets are generally formed from flame-flame interactions; however, flame pockets can appear from out-of-plane motion or by convecting into the image from the bottom of the frame. Flame pockets can either contain reactant or product gases and depending on the type of the pocket, their dynamics can be quite different. To capture their dynamic nature, a detailed tracking algorithm is implemented. A brief description of this algorithm is presented here: flame pockets in consecutive images are grouped and a convective distance threshold based on U and u' is used to predict the location of a pocket of interest in the consecutive frames. Once the location of the pocket in the consecutive frames is identified, an individual label is assigned to the pocket in each frame. These steps are followed until further tracking of the pocket is not possible. Figure 24(b) shows the rates of pockets ($\mathcal{R}_p$) for flame A - C for a period of one second. Results presented here show that similar magnitudes of pocket

rates are obtained for both reactant and product pockets for all flames. As noted previously, increasing turbulence levels increases the amount of wrinkling and the range of length-scales present in the flow, resulting in the increased pocket formation.

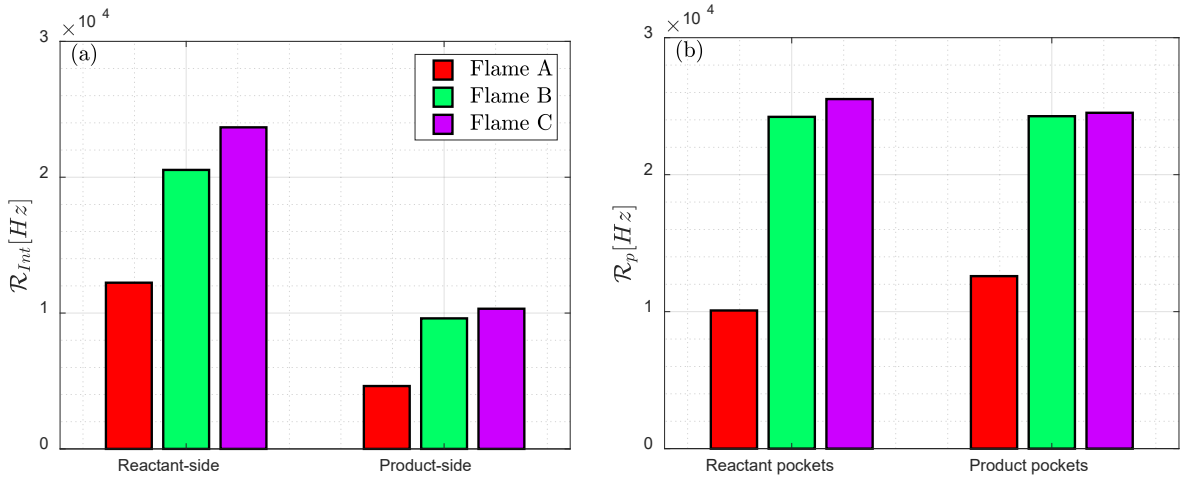

Figure 24: (a) Reactant- and product-side interaction rates ($\mathcal{R}_{Int}[Hz]$), and (b) rates of pocket formations ($\mathcal{R}_{p}[Hz]$) in flames A - C

A comparison between interaction rates and pocket rates shows that a similar number of reactant-side interactions and flame pockets occur for flames A - C, indicating that most reactant-side interactions form pockets. However, the product pocket rates obtained are almost twice as large as the product-side interaction rates for these flames. This anomaly suggests that more product pockets are observed in the plane of measurement compared to the product-side interaction events, which could be attributed to the out-of-plane motions present in this FOV. Figure 25 shows the PDFs of $\bar{c}$ at the locations of reactant- and product-side interaction events. The PDF plots for product-side interactions show peaks around $\bar{c}$ = 0.1 - 0.3, suggesting that product-side interactions mostly occur along the reactant side of the flame brush. On the other hand, the PDF plots for reactant-side interactions for flames A - C show that these interaction events are distributed over a wide range of $\bar{c}$ values. Inspection of OH-PLIF images shows that the width of the flame brush in this region is a result of large-scale flame motions, and that interactions occur at smaller length-scales on top of these large-scale motions. As such, the distribution of interactions is spread across a wide range in progress variable space. In the next section, these large-scale motions are identified and their effect on flame-flame interaction events are considered.

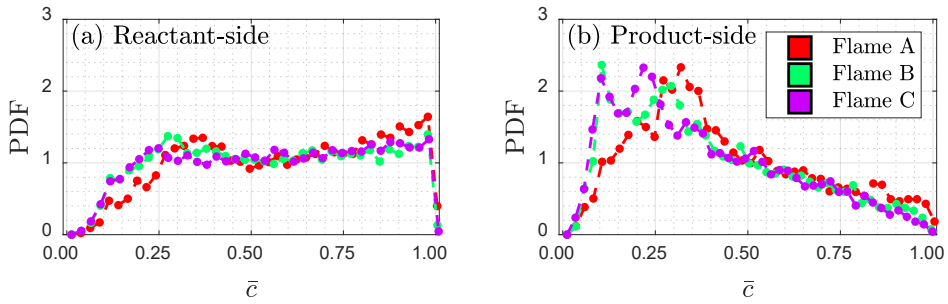

Figure 25: PDFs of $\bar{c}$ at flame-flame interaction locations for (a) reactant-side and (b) product-side flame-flame interactions

To identify coherent motions in the flames, the $\bar{c}$ fields are subtracted from the instantaneous binarized images (I_b) to obtain time-varying fluctuating images (I') for flames A - C, as described in Equation (6).

$$I'(t) = I_b(t) - \bar{c} \tag{6}$$

Using this Reynolds decomposition, a time-series of fluctuating intensity values for each pixel is obtained. A fast-Fourier transform of I' is performed to obtain the frequency spectrum of the flame fluctuation at every location. For this study, this Fourier analysis is performed at three probe locations in different regions of $\bar{c}$ fields, as shown by black dots in Figure 26. These locations are specifically chosen to capture large-scale motions along the inner branches of the left and right flames, as well as along the central part of the interaction zone.

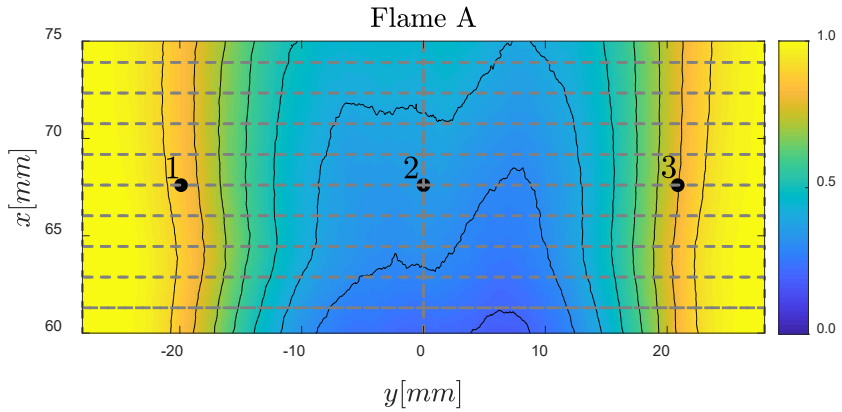

Figure 26: Probe locations for spectral analysis of flame front in inner flame branches and the interaction zone (black dots). Dashed gray boxes represent bins in vertical direction along the inner flame branches for the left and the right flames

Power spectral densities (PSDs) of I' for flames A - C at probe locations 1, 2, and, 3 are shown in Figure 27 (a), (b), and, (c), respectively. These results show strong oscillations in the inner flame branches at frequencies of 105 Hz, 140 Hz, and, 150 Hz for flames A, B, and, C, respectively. The interaction zone oscillations correspond to the first harmonic of the peak frequencies observed along the inner flame branches. Additionally, as the bulk flow velocity is increased, these peak frequencies also increase. Bénard von Kármán vortex shedding observed in bluff-body flows corresponds to a Strouhal number (*St*) in the range of 0.2 - 0.3 and for the peak frequencies identified here, the range of *St* is 0.026 - 0.052. This *St* range indicates that the strong oscillations that the flames undergo do not originate from vortex shedding behind a circular bluff-body and suggest that other coherent motions are present in the inner flame branches and the interaction zones.

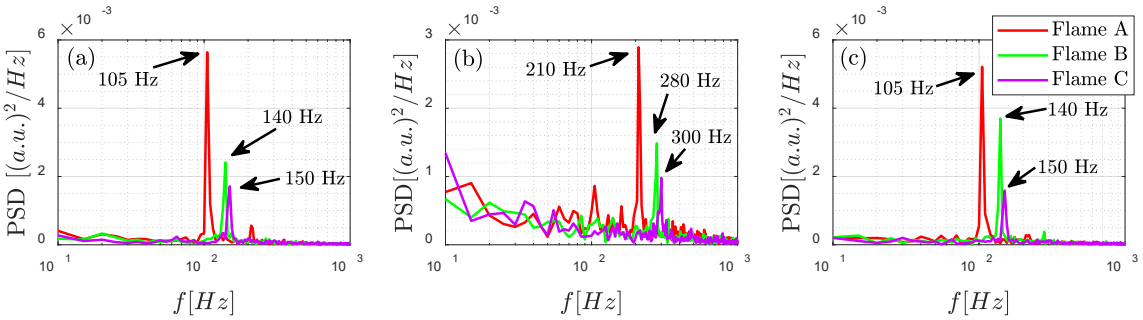

Figure 27: Power spectral densities of flame front fluctuations in (a) left flame inner branch, (b) interaction zone, and (c) right flame inner branch

To further investigate the nature of these oscillations, harmonic reconstruction of I' is performed to isolate motions corresponding to each peak frequency obtained from the Fourier analysis. This reconstruction is obtained by first calculating the amplitudes ($\mathcal{A}$) and phase angles (θ) of the fast-Fourier transform of $I'(t)$, obtained from the expression shown in Equation (7):

$$\hat{I}(f) = \mathcal{A}\exp(-i\theta) \tag{7}$$

The harmonic reconstruction at a frequency of interest is calculated using Equation (8):

$$\tilde{I}_{|f=f_0}(t) = \Re\{\mathcal{A}(f)\exp(-i\theta(f))\exp(-2\pi i f t)\} \tag{8}$$

Here, $\Re$ corresponds to the real-part of the expression. The image reconstruction is done over a limited region of the full image, shown in Figure 26. To increase the computational speed for reconstructions, images are down-sampled by a factor of 16 and $\hat{I}(f)$ and $\tilde{I}(t)$ are obtained at each "super-pixel" location. This down-sampling results in a resolution of 1.6 mm/pixel. Figure 28 shows one cycle of harmonically reconstructed oscillations at frequencies of 105 Hz and 210 Hz for flame A. These images show convective oscillations that span greater than half of the height of the FOV. Specifically, in the case of 105 Hz (Figure 28 (a)), complete out-of-phase oscillations occur in the inner branches for both flames. These oscillations are not present in the outer flame branches of these flames (not shown), which indicates that the interaction between these flames strongly affects the flame branches in the interaction zones. Similar to flame A, these convective out-of-phase oscillations are also present in flames B and C at peak frequencies of 140 Hz and 150 Hz, respectively.

Flame-flame interaction events can be conditioned on the inner flame branches to directly investigate the effect of large-scale motions of the flame branches. This is achieved by creating interrogation windows along the x-direction for each flame branch and assigning whether the interaction occurs along the inner branch of the left or the right flame. The size of the interrogation windows is set at 16 pixels in the vertical dimension, resulting in a resolution of 1.6 mm. These interrogation windows are shown in gray dashed-lines in Figure 26. Since flame-flame interactions can occur over a wide range of scales, the centroids of the shapes of the interactions are used to obtain a single mean location in the x-direction. These centroid locations are used to populate the interrogation windows and the spatial variation of flame-flame interaction events are obtained; these results are presented in Figure 29(a) and (b). For all flames, reactant- and product-side interactions are counted separately along the inner flame branches. Results for the reactant-side interactions show that in the current FOV, counts of interaction events tend to increase in the range of x = 55 mm - 62 mm and then decrease from x = 63 mm - 72 mm. The trends between the left and the right

flame branches are similar to each other and for all flames shown here. For product-side interactions, differences exist between flame A and flames B and C; interaction counts for flame A show a peak near x = 64 mm, while two peaks occur near x = 57 mm and 67 mm for flames B and C. These results along the inner flame branches suggest that for reactant-side interactions, an increase in inlet Reynolds number only affects the intensity of these interactions and not their spatial distributions, On the other hand, for product-side interactions, the intensity, as well as the spatial distribution, are changed due to the increase in inlet Reynolds number.

To link the large- and small-scale motions, time series of the interaction event counts are extracted for each interrogation window along the inner flame branches; an example of such a time-series is shown in Figure 29(c). While the interactions may seem intermittent, there is a connection between the time-scales of interactions and the large-scale frequencies shown in Figure 27. Arrival frequencies of interaction events are calculated by evaluating the time delay between the occurrence of consecutive interaction events (Δt_{int}) in an interrogation window location. These time-scales are inverted to obtain an arrival frequency (f_a), as shown in Equation (9):

$$f_a = 1/\Delta t_{int} \quad \textbf{(9)}$$

This analysis is performed at all interrogation window locations and for reactant- and product-side interaction events. Histogram maps of arrival frequencies as a function of downstream location are shown in Figure 30. The left column in this figure correspond to reactant-side interactions and the right column corresponds to product-side interactions. The histogram maps show that reactant-side interaction events occur for a wide range of f_a values in both inner flame branches. It is also interesting to note that near x = 62 mm, the range of f_a is broad, indicating a large number of interactions occurring for flames A - C as previously highlighted in Figure 29. The broadband distribution of interaction frequencies is likely driven by turbulent flame wrinkling. Additionally, a high number of lower frequency interactions in the ranges of 100 Hz - 500 Hz suggests that the large-scale oscillations corresponding to 105 Hz, 140 Hz, and 150 Hz may drive the occurrence of reactant-side interactions in both flame branches. Similarly, for product-side interactions, a majority of f_a values fall in the low frequency ranges (100 Hz - 500 Hz), suggesting that large-scale flame motions play a role in facilitating interactions.

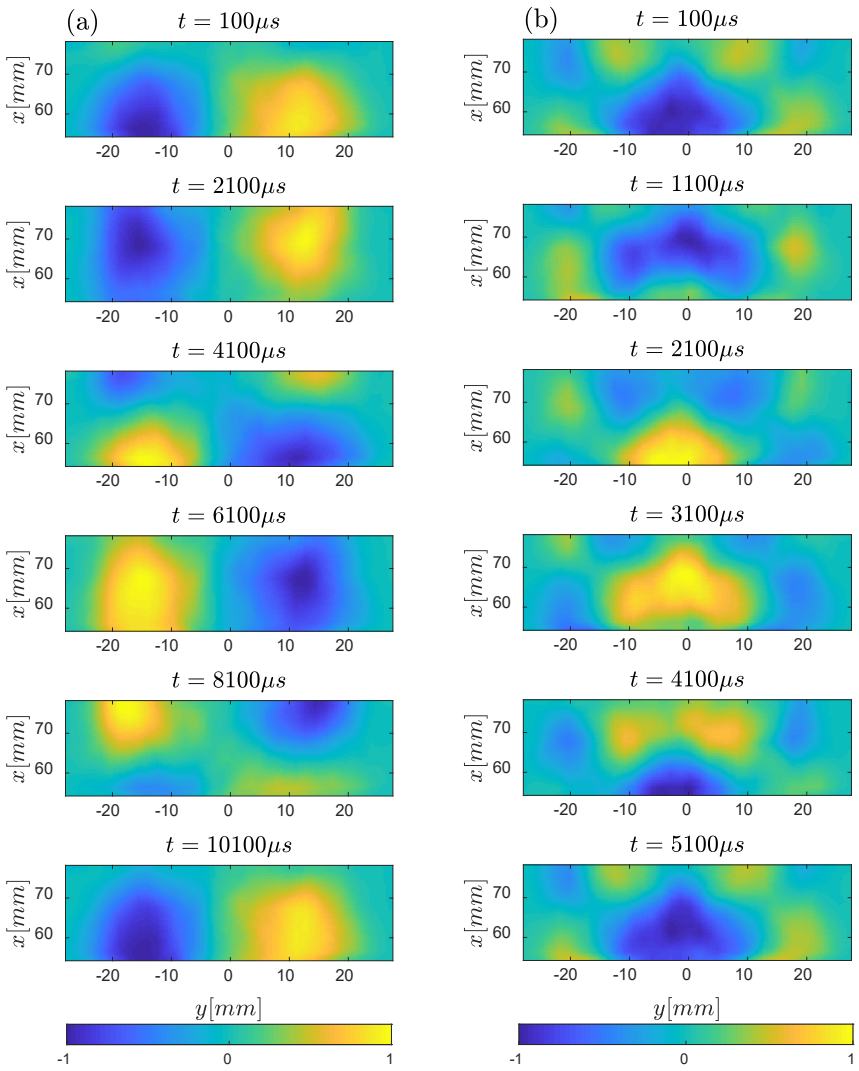

Figure 28: Time-series of harmonically reconstructed large-scale flame motions at (a) 105 Hz and (b) 210 Hz for flame A

These results suggest that while local turbulence and flame wrinkling can be the primary mechanisms leading to flame-flame interactions, large-scale oscillations are equally important in the occurrence of these interactions. The connection between flame annihilation events and large-scale motions aligns with previous studies on thermoacoustically unstable systems, where large-scale flame oscillations affect the spatial distribution of flame-flame interaction events. Higher arrival frequencies for reactant-side interactions are present in closely packed regions along the x-direction, while lower arrival frequencies are present along a wide range of x-locations. Similarly, the lower arrival frequencies for product-side interactions are widely distributed along the x-direction. This finding connects the large-scale global behavior to the sub-grid level behavior of turbulent flames.

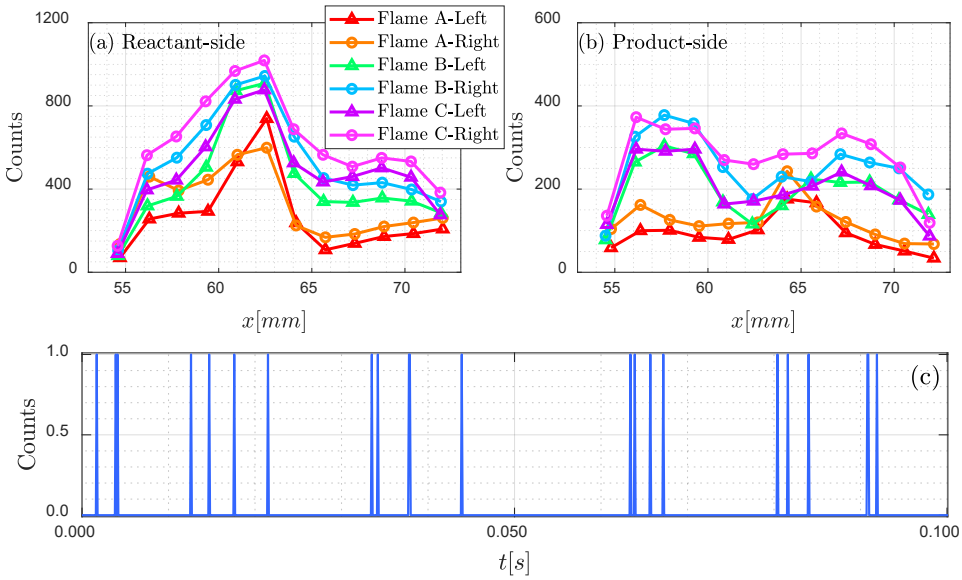

Figure 29: Flame-flame interaction counts for 16-pixel interaction regions along the inner branches of left and right flames: (a) reactant-side and (b) product-side. (c) Example of the time-series of counts of reactant-side interactions at an interrogation window in the inner branch of the left flame

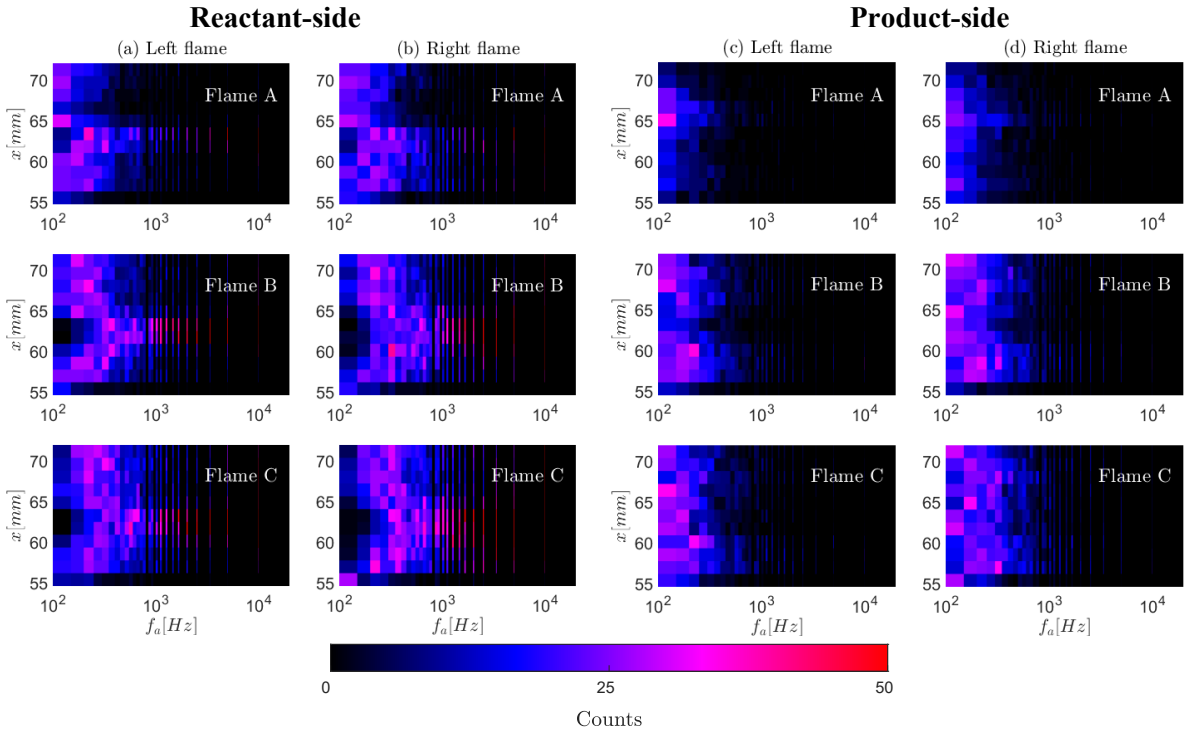

Figure 30: Arrival frequencies for reactant-side flame-flame interactions along the inner branches of: (a) left and (b) right flames. Left column: reactant-side interactions, right column: product-side interactions

6 Role of pocket formation on flame surface dynamics

6.1 Publications from this effort

- Tyagi, A., Boxx, I., Peluso, S., & O'Connor, J. (2020) "Pocket formation and behavior in turbulent premixed flames," *Combustion and Flame,* **211**, pg. 312-324.

6.2 Effect of pockets on global flame structure

Pocket formation is an important characteristic of turbulent premixed flames and understanding pocket behavior is key to developing high-fidelity numerical combustion models. In this study, a dual-burner experiment is used to study pockets in single- and dual-flame configurations and synchronized high-speed OH-planar laser-induced fluorescence and stereoscopic-particle image velocimetry imaging techniques are implemented to track flame pockets and the surrounding flow field. Figure 31 (a) shows the stitched flame surface density (FSD) of case A-Single from all three FOVs. Flame surface density is calculated using an interrogation window size of 1 x 1 pixel with a pixel resolution of 0.1 mm/pixel. Flame edges are counted in these interrogation windows for 10,000 images and the average signal in each interrogation window is divided by the window area to obtain FSD. This image shows that FSD is high at the base of the flame and decreases with downstream distance as the flame brush thickness increases. The impact of flame pockets on the time-averaged flame structure is quantified by calculating the FSD neglecting the surface contribution from the pockets. This new FSD is subtracted from the total FSD to quantify the impact that flame pockets have on global flame structure. These results are shown in Figure 31 (b)-(d) for case A-single; the colorbar in all figures is adjusted to highlight the FSD differences in these images. Figure 31 (b) shows the difference in FSD with all the pockets subtracted, whereas Figure 31 (c) shows the difference in FSD with just the reactant pockets subtracted. These images are similar, indicating that the pockets do not have a large effect on FSD near the base of the flame but contribute a more significant portion where flame tip pinching is present. Similar spatial distributions of reactant pocket formation and burnout were observed by Worth and Dawson [32], showing that reactant pockets are more likely to form near the tip. Figure 31 (d) shows the difference due to the lack of product pockets, where product pockets are more likely to form near the base of the flame and do not account for a significant portion of the FSD. Altogether, these results indicate that flame pockets contribute to 10-20% of the total flame surface, depending on operating condition.

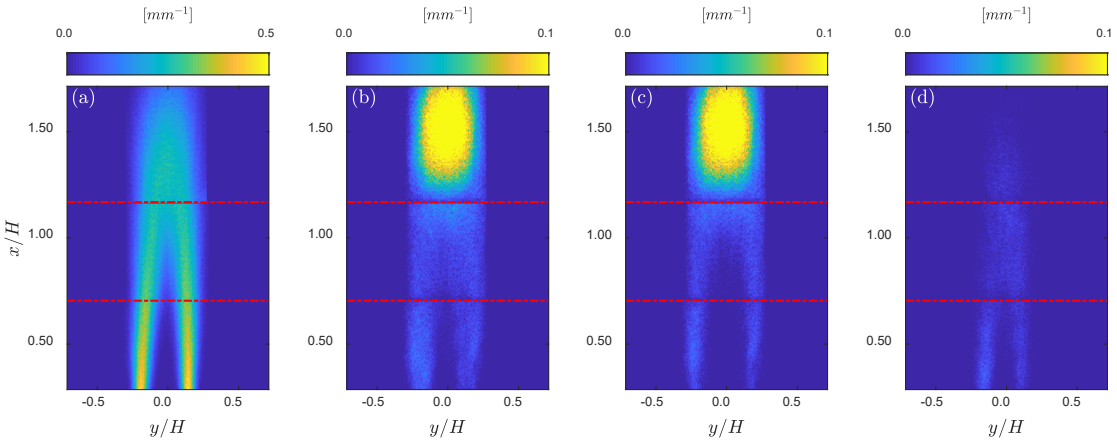

Figure 31: Flame surface density contributions for flame A-Single: (a) total, (b) all pocket contributions, (c) reactant pocket contributions, and (d) product pocket contributions

6.3 *Pocket formation rates*

Figure 32 shows the formation rate of reactant and product pockets ($\mathcal{R}_{R,p}$ and $\mathcal{R}_{P,p}$) in units of Hertz for both single and dual flames. In each sub-figure, the rate is calculated per FOV and plotted against the mid-point of the vertical location of the FOV normalized by the flame height. The flame height is calculated based on the height of the time-averaged progress variable contour of $\bar{c}$=0.2. Additionally, the results plotted in these sub-figures for dual flames cases are averaged between the two flames to make direct comparisons with single-flame cases. We expect that as high as 98% (in low turbulence cases) and as low as 81% (in high turbulence cases) of the identified interactions are the result of in-plane motion as opposed to out-of-plane motion.

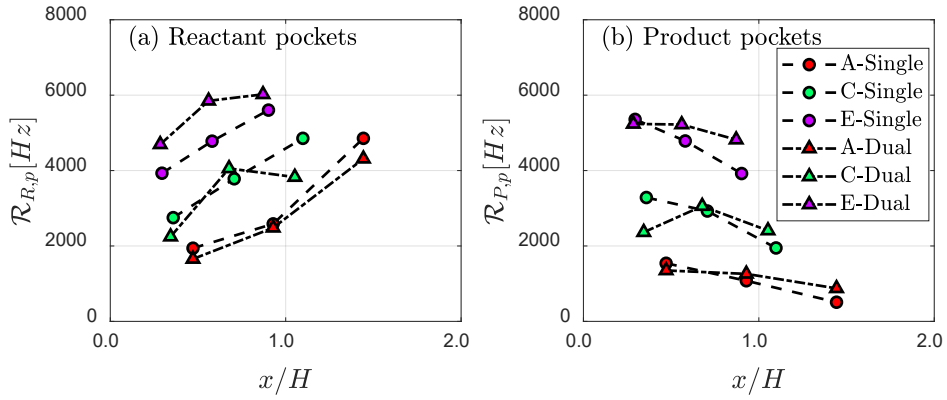

Figure 32: Frequency of pocket formations in [Hz] for: (a) reactant pockets, (b) product pockets

Reactant pocket formation rates (Figure 32 (a)) increase with downstream distance for both single- and dual-flames cases. As the bulk flow velocity increases, the rate of reactant pocket formation also increases, indicating that higher turbulence levels increase wrinkling of the flame front, resulting in increased tendency of the flame to pinch-off and form pockets of reactant gases. These findings are congruent with the FSD plots shown in Figure 31. For cases A-Single and A-Dual, an abrupt increase in the reactant pocket formation is seen in FOV III (corresponding to x/H=1.4). This FOV captures the flame tip region for these flames and more reactant pockets are observed to be formed in this region due to flame pinch-off, as shown by Figure 31 (b).

The product pocket formation rates presented in Figure 32 (b) show that product pockets tend to form in the upstream regions of the flame. Product pocket formation is more frequent when large strain rates are present on the reactant side of the flame surface; this strain can dominate flame propagation and result in splitting of product gases from the main flame [6, 33]. The increase in the bulk flow velocity also increases the turbulent fluctuation intensity and high strain rates can be present in these flames, resulting in increased product pocket formation for cases C and E (in both single- and dual-flames). Additionally, as the turbulence level decreases with downstream distance (see Figure S11 in the supplementary material), the product pocket formation rates also decrease; note that these trends may be less significant given the up to 20% uncertainty associated with identifying interaction events. Trends for reactant and product pocket formations as a function of downstream distance shown in Figure 32 (b) match well with the FSD plots shown in Figure 31. Comparisons between single- and dual-flame cases show that pocket formation rates are very similar for both configurations. These pocket formation rates closely follow the interaction rates, where reactant-side interactions increase frequency with downstream distance and product-side interactions decrease frequency with downstream distance.

Histograms of the original size of each pocket are shown in Figure 33; the size is quantified as the mean radius of the pocket, which is calculated by first identifying the center of mass of the pocket (assuming

constant density inside) and then averaging the radii along the length of the pocket perimeter. The integral length scale and the Taylor microscale, calculated at the exit of the burner, are provided for reference in each case. In the first two FOV, reactant and product pockets have similar size distributions. In FOV III, the reactant pocket distribution has a tail of larger radius pockets that are indicative of the pinch-off of large pockets at the tip of the flame. In general, most of the pockets are smaller than both the integral length scale and the Taylor microscale, indicating that these pocket formations may be occurring on the sub-grid in many large-eddy simulations (LES). Despite their small size, we show in the next section that these pockets are formed quite frequently, making the dynamics of these pockets a significant contributor to local flame surface dynamics.

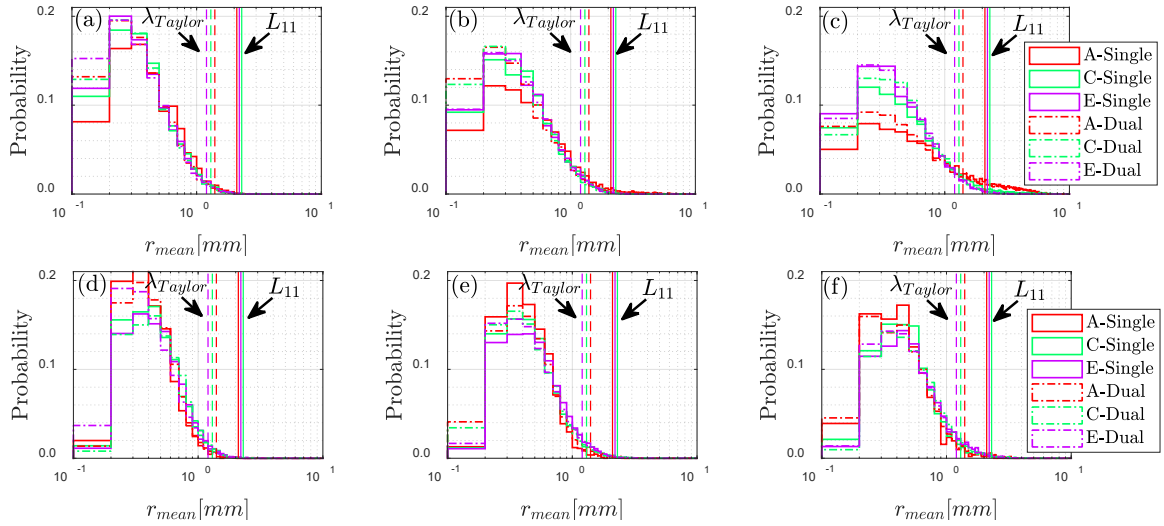

Figure 33: Mean pocket radii for reactant pockets in (a) FOV I, (b) FOV II, and (c) FOV III. Mean pocket radii for product pockets in (d) FOV I, (e) FOV II, and (f) FOV III

6.4 Pocket origin and fate

Figure 34 shows the origin of reactant and product pockets for single and dual flames in FOVs I-III. Reactant pockets are most likely to originate from flame-flame interaction events and very few reactant pockets appear from out-of-plane. Additionally, the probability of reactant pockets being formed from observed flame-flame interactions increases as the downstream distance increases along the flame, which aligns with the reactant pocket formation rate results (Figure 32). The majority of the product pockets appear from out-of-plane and very few pockets originate from flame-flame interactions observed within the plane of measurement (Figure 34 (b)). The fact that most reactant pockets originate from interaction sites provides further confidence that the detected pockets are, indeed, actual pockets and not three-dimensional motions. The fact that most product pockets appear from out of plane, and not from interaction sites, is the reason for our lower confidence in identifying these product islands as product pockets. However, there is currently no method for separating these two types of product islands in a planar measurement and so we continue to analyze them as both pockets and through-plane events.

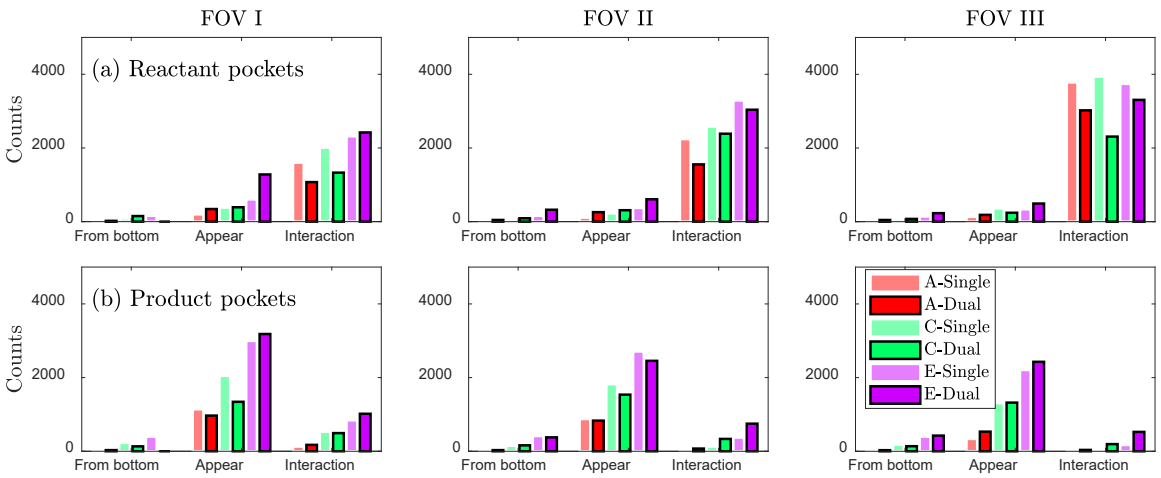

Figure 34: Statistics of pocket origin: (a) reactant pockets, (b) product pockets in the measurement plane

The local impact of pockets on the main flame can be captured by tracking the fate of pockets. For example, pockets can either burn out or merge with the main flame, locally altering the consumption of reactants and the local topology of the flame. Figure 35 (a) shows the statistics of reactant pocket fate in FOVs I-III. Results show that most reactant pockets burn out; a smaller number of pockets move out of the FOV and their fate remains unknown. A small number of reactant pockets merge with the main flame surface. Merging of reactant pockets with the main flame surface can result in perturbations to the flame surface area and consequently to the local heat release rate. Increasing the bulk flow velocity also increases the frequency of reactant pocket formation, resulting in increasing frequency of all pocket fates by a similar fraction. Note that the size of the FOV affects the balance of these histograms for both pocket origin and fate; a larger field of view would result in fewer "moved out" pockets, for example.

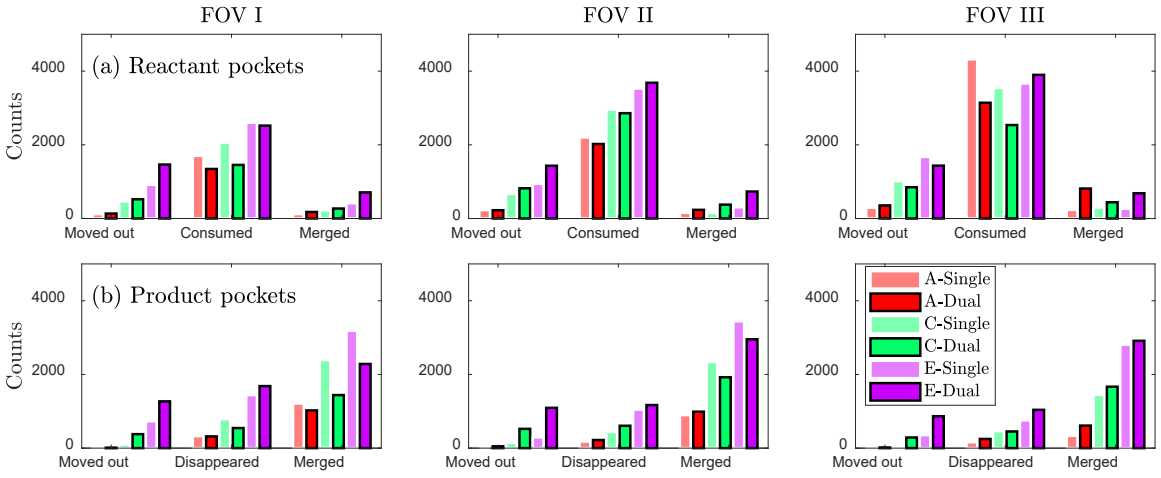

Figure 35: Statistics of pocket fate: (a) reactant pockets, (b) product pockets in the measurement plane

7 Role of piloting on turbulent flame behavior

7.1 Publications from this effort

- Tyagi, A., Shupp, R., Breseler, K., O'Connor, J. "The effect of back-support piloting on turbulent flame structure and hole formation." *Combustion and Flame*, **in preparation**
- Beseler, K., Tyagi, A., O'Connor, J. (2020), "Development of a diagnostic Damkohler number for interpreting laser-induced fluorescence data in turbulent flames," *AIAA SciTech Forum,* Orlando, FL
- Shupp, R., Tyagi, A., Boxx, I., Peluso, S., O'Connor, J. (2018). "The effects of piloting on turbulent flame structure." *Technical Meeting of the Eastern States Section of the Combustion Institute*, State College, PA.

7.2 Effect of piloting on global flame structure

To quantify the impact of piloting on global quantities such as flame brush thickness and global consumption speed, the burner was run with three different pilot configurations, each over three bulk flow velocities of 12 m/s, 20 m/s, and 28 m/s. The piloting configurations consisted of a condition where both anchoring and back-support pilots were used (denoted as "AB"), a condition where only anchoring pilots were used (denoted as "A"), and a condition where only back-support pilots were used (denoted as "B"). The test matrix in Table 4 provides the details of each of the nine cases examined; the main flame and all pilot flames had an equivalence ratio of 1 at all conditions.

Table 4. Test matrix for global behavior study.

Case	U [m/s]	Re_D	Pilot
12AB	12	15485	All
12A	12	15485	Anchoring
12B	12	15485	Back-support
20AB	20	25808	All
20A	20	25808	Anchoring
20B	20	25808	Back-support
28AB	28	36131	All
28A	28	36131	Anchoring
28B	28	36131	Back-support

Figure 36a shows stitched, time-averaged progress variable plots with red lines separating the three fields of view used for data collection. As bulk flow velocity increases, the height of the flame increases, as expected. The progress variable contours on the reactants-side of the flame look similar in all three cases. Differences in the product-side contours are the result of the pilot flames. In AB and B, where the back-support pilots are present, a wide OH layer from the back-support pilot flame surrounds the main flame, which can also be seen in the instantaneous OH images in Figure 36b. However, with an anchoring-only configuration (A), the products-side contour at the base of the flame is different in the absence of that OH layer. This omission is particularly noticeable at the higher velocities. At the highest velocity, the peak time-averaged progress variable near the base of the flame is no longer unity, indicating incomplete combustion in that region. The presence of flame holes is evident in the instantaneous OH-PLIF image in Figure 36b, and it is these flame holes that drive the incomplete combustion in this region.

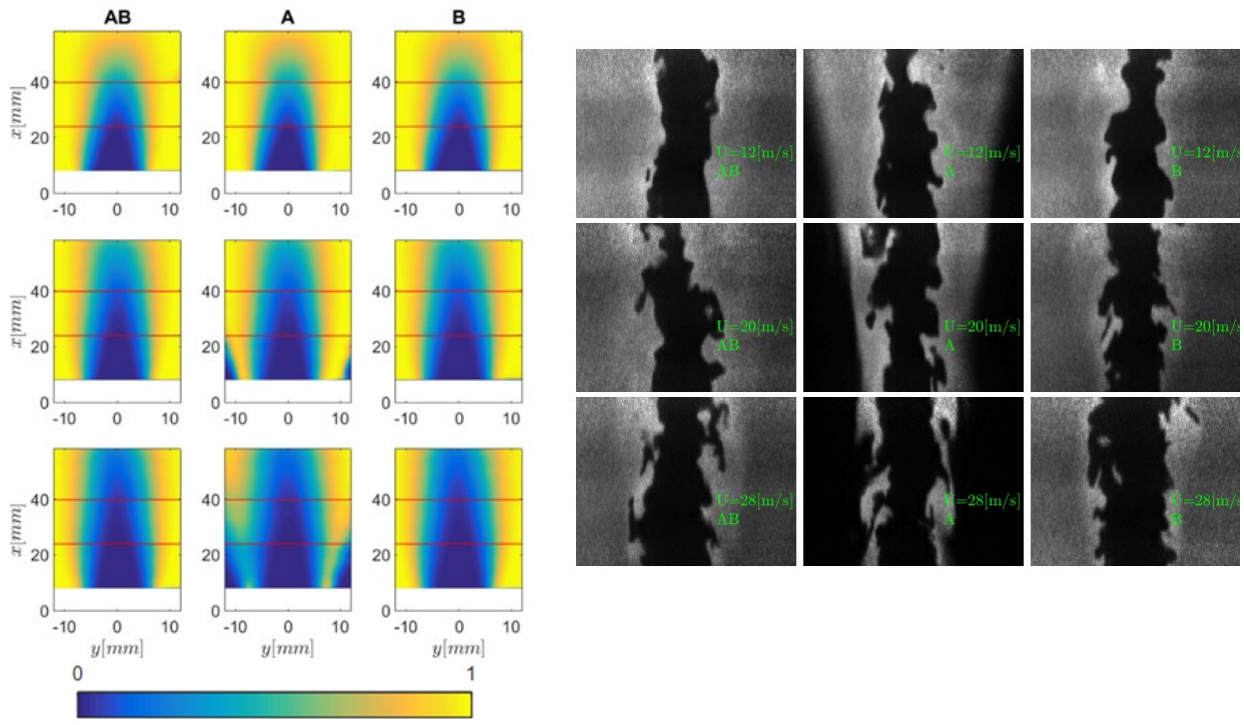

(a) **(b)**

Figure 36. Stitched, time-averaged progress variable contours (a) and instantaneous OH-PLIF images (b) for the nine cases.

Figure 37 shows the flame brush thickness as a function of downstream distance for all three conditions. The magnitude of the flame brush thickness was calculated as $\delta_t = \max\left(\frac{1}{\left|\frac{\partial \tilde{c}}{\partial y}\right|}\right)$. Despite the differences in the absolute value of the time-averaged progress variable contours at condition A vs. conditions AB and B, the flame brush growth is similar in all three cases. This similarity is driven by the fact that the flame brush definition is gradient based, rather than based on the absolute value of the progress variable. As the flame brush development is largely driven by the turbulence development in the flow field, it is expected that the brush thickness would be similar in all piloting cases.

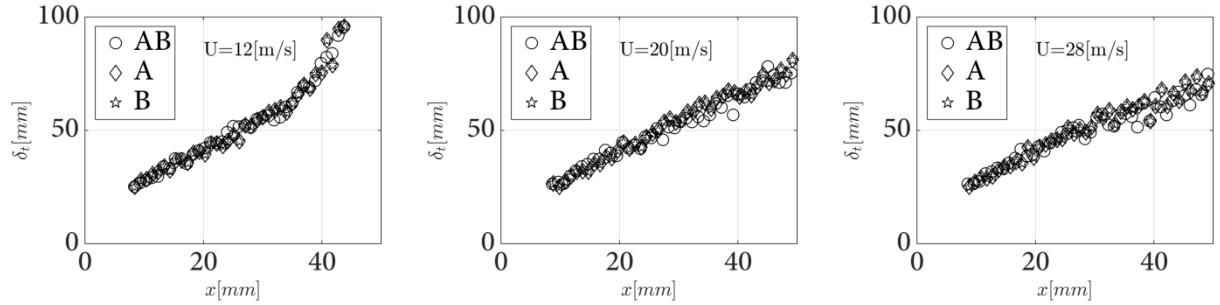

(a) 12m/s ***(b) 20m/s*** ***(c) 28m/s***

Figure 37. Flame brush thickness vs. position for bulk flow velocities of (a) 12 m/s, (b) 20 m/s and (c) 28 m/s.

Interestingly, the global turbulent consumption speed is also not significantly different in these three piloting cases. Figure 38 shows the global consumption speed, calculated as $S_{T,GC} = \frac{\dot{m}_R}{\rho_R A_{\bar{c}}}$, where the area of the flame is calculated using three different progress variable contours – $\bar{c} = 0.1, 0.2, 0.3$. The lack of difference in the global consumption speed is indicative of two things: the definition of consumption speed based on reactants-side progress variables and the averaging of instantaneous dynamics inherent in the global consumption speed definition. As the reactants-side progress variables are similar in all piloting configurations, one would expect that the global consumption speed would also be similar; definitions based on the products-side progress variables would vary greatly but also are indicative of the layers in which the fuel is being consumed and therefore would provide non-physical answers. Further, the time-averaging process reduces the impact of instantaneous extinction events, which significantly vary with piloting configuration.

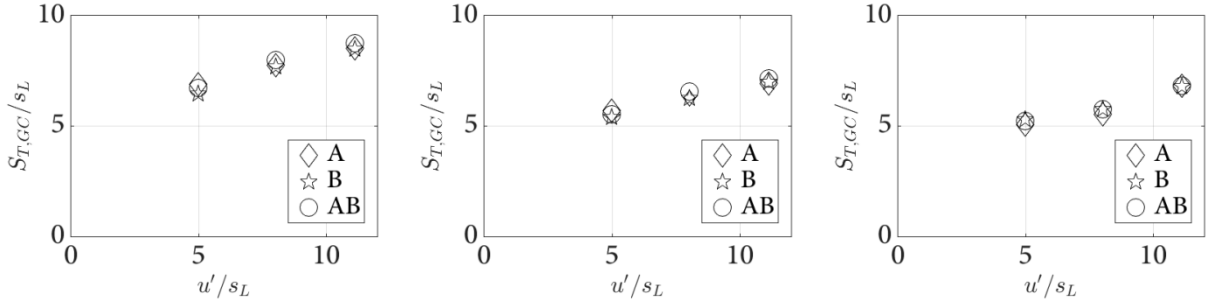

$(\boldsymbol{a})\ \bar{\boldsymbol{c}} = \mathbf{0.1}$ $(\boldsymbol{b})\ \bar{\boldsymbol{c}} = \mathbf{0.2}$ $(\boldsymbol{c})\ \bar{\boldsymbol{c}} = \mathbf{0.3}$

Figure 38. Turbulent global consumption speeds for progress variables of (a) 0.1, (b) 0.2 and (c) 0.3.

Despite the similarity in the global quantities at the three piloting conditions, inspection of the flame structure at the highest flow velocity, shown in Figure 36b, indicates that the *instantaneous* structure of the flame is significantly different in the absence of piloting, particularly back-support piloting. To this end, we inspect the instantaneous structure of the flames as measured by high-speed OH-PLIF images.

7.3 Effect of piloting on flame extinction

Back-support pilot flames produce a layer of hot products parallel to the flow of the premixed reactants. These parallel flows mix across a diffusion layer and that diffusion layer mixing can be modeled using asymmetric counterflow jets. In the asymmetric counterflow configuration, one jet is composed of hot products and the opposite jet is composed of reactants. At the stagnation plane of the two jets, the products and reactants mix across the diffusion layer, thus mimicking back-supported flames. The asymmetric configuration includes a jet of premixed methane-air reactants and a jet of burned products from a stoichiometric methane-air flame. The velocity of the jets is varied but kept symmetric to create a range of steady strain rates. Data on the location and mole fraction of various species are tracked along with the reaction rates of key reactions.

From the s-PIV measurements, strain rates can be extracted ahead of the flame front region. For the purpose of the current study, a time-averaged progress variable location of 0.1 is chosen to calculate strain rates in the Cartesian frame of reference using the following equations:

$$S_{ij} = \begin{cases} S_{12} = \frac{1}{2}\left(\frac{\partial U_x}{\partial y} + \frac{\partial U_y}{\partial x}\right) \\ S_{11} = \frac{\partial U_x}{\partial x} \\ S_{22} = \frac{\partial U_y}{\partial y} \end{cases} \quad \textbf{(2)}$$

Figure 39a shows the location of the progress variable in a dual-flame configuration, which has been discussed in our previous work [18]. Figure 39b shows the probability density function (PDF) of instantaneous strain rates along the $\bar{c}$=0.1 contour, indicating that the highest strain rates measured were on the order of 5000 1/s; this range of strain rates is used in the OPPDIF simulation. These very high levels are strain are evidence of the significant role that back-support pilot flames play in stabilizing the flame and maintaining the flamelet structure in operational regimes where traditional theory like the Borghi-Peters diagram would predict broken flamelets.

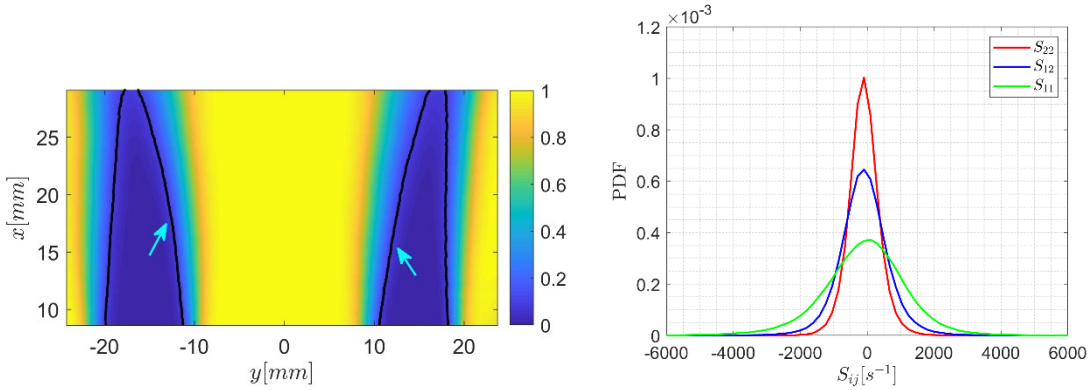

(a) (b)

Figure 39. (a) Time-averaged progress variable of dual-burner flames operating at U = 12m/s. The black-contours represent the $\bar{c}$=0.1. (b) PDFs of strain rates along the $\bar{c}$=0.1 of the left flame

Using Chemkin's OPPDIF model, key features for each of the cases can be extracted. The peak heat release rate for each bulk strain case is shown Figure 40. As the bulk strain increases, the peak heat release rate decreases. However, even at very high strain rates, the peak heat release rate does not reach zero as would be expected with flame extinction. The peak heat release rate appears to asymptote to approximately 250 J/cm^3/s at high strains, which is over an order of magnitude less heat release than in the unstrained case. This sustained heat release suggests that even at very high strains, reactions are continuing to occur and would be visible using a LIF diagnostic like OH- or CH-PLIF. There is a lack of clear extinction even at very high strain rates. The continued reactions at high strains and shift in location to the burned products zone could be attributed to the pool of radicals supplied by the burned products. The burned product temperature combined with the radicals could be enough to create a pseudo preheat zone where the strain rates are too high for a preheat zone to normally exist. This pseudo preheat zone could be enough to keep the combustion reactions going even at strain rates where extinction should be occurring.

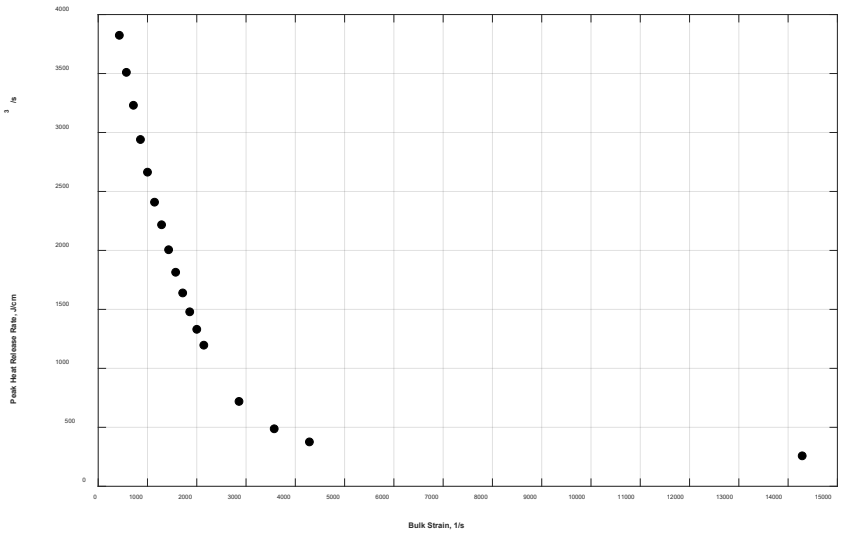

Figure 40. Peak heat release rate as a function of bulk strain

8 Method for estimating out-of-plane effects

8.1 Publications from this effort

- Tyagi, A., O'Connor, J. (2020), "Towards a method of estimating out-of-plane effects on measurements of turbulent flame dynamics," *Combustion and Flame*, **under review**

8.2 Background

The use of planar laser diagnostics for measurement of premixed turbulent flames is ubiquitous. The increased availability of high-speed planar laser-induced fluorescence (PLIF) systems for identifying species such as OH, CH, CH_2O, and others has allowed a large number of researchers to investigate the structure and dynamics of flames. In particular, the use of OH- and CH-PLIF for tracking flame edges has been used in a wide variety of premixed flame studies. Though these studies have significantly enhanced our understanding of turbulent flame dynamics, there is still uncertainty as to the impact of out-of-plane behavior on the interpretation of results measured in plane. The goal of this work is to propose a framework by which theory and probabilistic modeling can be used to estimate the contribution from out-of-plane effects. We limit ourselves, initially, to measurement of turbulent flame dynamics, rather than measurement of chemical kinetics.

There are several out-of-plane effects that can arise in the measurement of turbulent flame dynamics. As turbulent flames are inherently three-dimensional, measurement of the flame surface in a plane will not capture its rich topology. A similar issue arises with the definition of flame curvature, which requires the calculation of gradients in three-dimensional space. The measurement of displacement speed also suffers in a planar measurement as the normal to the flame cannot be rigorously defined. The measurement of consumption speed is affected by planar measurements as the area of the flame measured in the laser plane may not be representative of the total surface area of the flame, making a calculation of mass flow rate through the surface difficult.

Data from our planar turbulent Bunsen flame is in Figure 41, which shows PDFs of the consumption speed of flame pockets. These pockets were tracked through space and their consumption rate calculated by knowing the pocket area and perimeter in the plane of the laser: $S_C = \Delta A / P_1 \Delta t$. In a 3D sense, consumption speed can be calculated by $S_{C,3D} = \Delta V / S_a \Delta t$, which requires knowledge of both the volume and surface area of the flame at any given time. The 2D formulation approximates the 3D form but can be

biased by the region of the pocket that is captured in the plane of the laser. Even in a statistical sense, the consumption speed calculations have an issue, which is evidenced in the PDFs in Figure 41. These PDFs show that some percentage of the pockets have a negative consumption speed, which is not physical for reactant pocket consumption at the turbulence intensities present in this experiment (u'/s_L=5.5 – 12.6). We believe that the negative consumption speeds are an artifact of making a planar measurement of a three-dimensional object. As such, the measured consumption rates are actually a combination of actual consumption speeds and apparent consumption speeds due to the planar measurement.

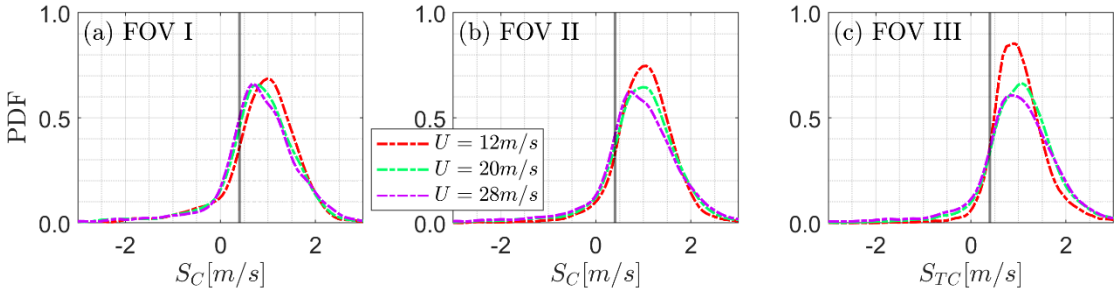

Figure 41. PDFs of reactant pocket consumption speeds in field of view (FOV) (a) I, (b) II, and (c) III for single Bunsen flames. Vertical lines represent s_L=0.4 m/s

8.3 Approach

The goal of this formulation is to more accurately calculate the consumption speed of a flame pocket, although the procedure could be applied to any out-of-plane effect. Figure 42 shows a flowchart depicting the methodology implemented in this analysis. The measured consumption rate distribution is assumed to be a mixture of two distributions (distributions 1 and 2) that represent consumption rates from out-of-plane motion and true consumption rates, respectively. In order to calculate the distribution of out-of-plane consumption rates, the 3D pocket shapes are estimated from measured 2D edges. Measured out-of-plane velocities from s-PIV are used to simulate convection of reactant 3D pockets through a stationary plane and cross-sectional pocket areas and perimeters are calculated. These geometric parameters are used to calculate the apparent reactant pocket consumption rate due to through-plane pocket convection. A PDF of this apparent consumption rate is obtained and this PDF is separated from the measured consumption rate PDF to obtain a corrected PDF, allowing for estimation of the uncertainty due to pocket convection.

Statistics from the pocket construction analysis are presented in Figure 43; Figure 43(a) shows the histogram of mean pocket radii for pockets identified from OH-PLIF measurements. It is important to note that the UV laser sheet height restricts completely tracking large-radii pockets through burnout. However, most pockets have small radii and hence we observe the full burn-out of most pockets. Additionally, the size of most of these pockets is smaller than the integral length scale and the Taylor microscale from the incoming turbulence at the burner exit. In Figure 43(b), histograms of the spatially-averaged out-of-plane velocities within reactant pockets are shown. This histogram is not symmetric about zero, indicating that some bulk out-of-plane velocity exists and can drive pockets into and out of the measurement plane. In Figure 43(c), the histogram of the maximum Legendre polynomial used for fitting r_p is presented. Using the criterion set earlier with finding n that matches a P_{coeff} of 0.9, most of these pockets are fitted with Legendre polynomials of orders $n_{max} < 7$.

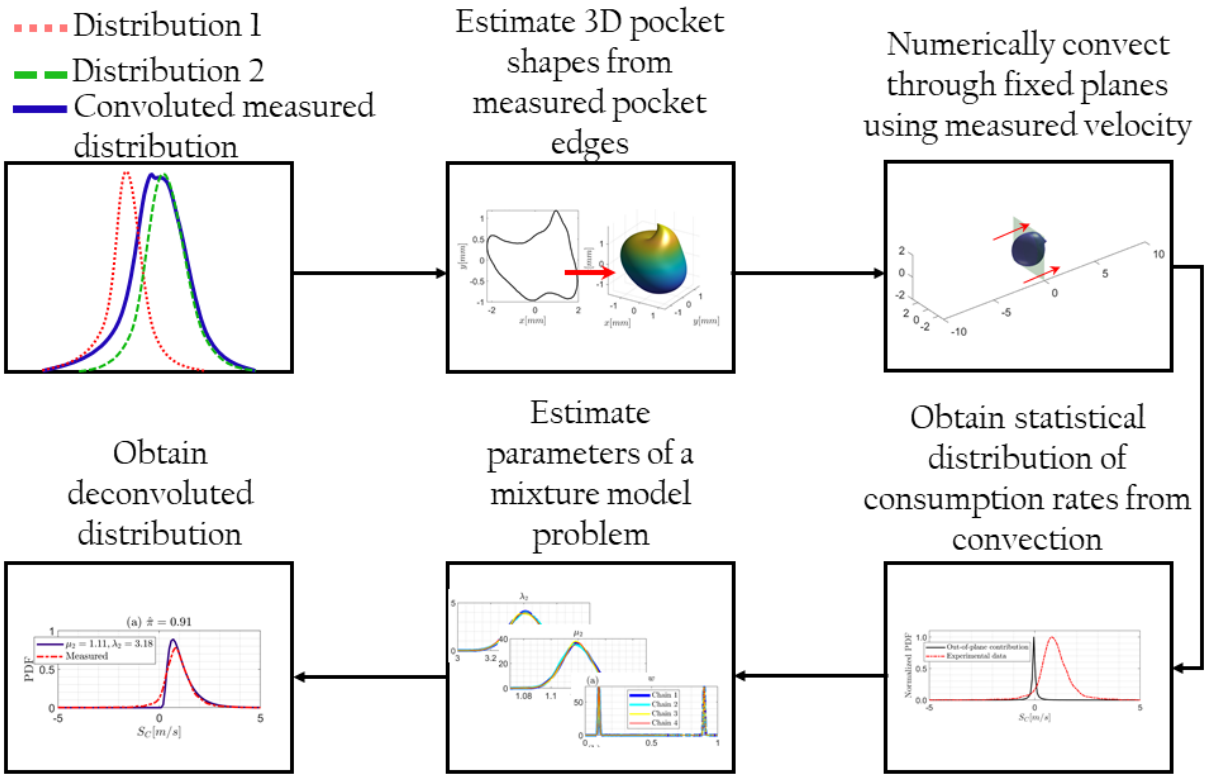

Figure 42. Flowchart of the framework for obtaining true consumption rates from measured consumption rates

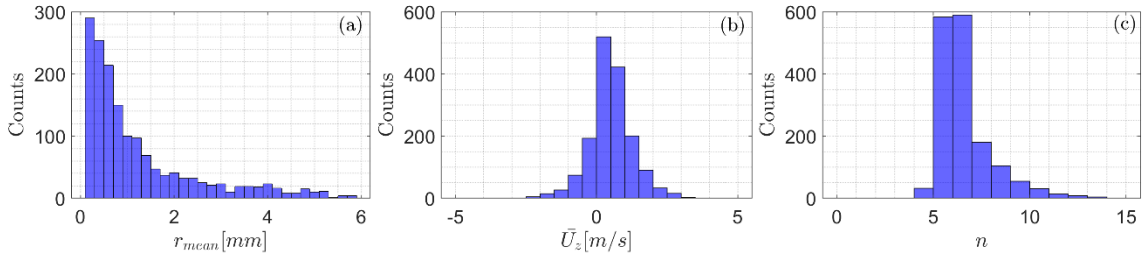

Figure 43. Histograms of (a) mean pocket radii (r_{mean}), (b) mean out-of-plane velocities inside pockets, and (c) maximum value of n_{max} used.

Figure 44 shows the probability densities of w, μ_2, and λ_2 from the MCMC simulations; figures in each row show the probability densities from four example Markov chains for w, μ_2, and λ_2. These plots show that all Markov chain results are converged and provide roughly the same solution for these variables. Table 5 shows the median values of μ_2, λ_2, and $\hat{\pi}$. Since pocket mean radii exist across a wide range of scales, the result presented here are decomposed based on the mean radii belonging to three categories: $r_{mean} \in [0, 2]$ mm, $r_{mean} \in [2, 4]$ mm, and $r_{mean} > 4$ mm. Results for these different ranges show that the mean of the true distributions ranges from 0.92 - 1.13 and the scale metric ranges from 2 - 3.91. The mixing value of the mixture models ranges from 0.9 - 0.94, indicating that the true distributions are largely made up of points from the measured distributions. This is expected because a relatively small percentage of consumption rates are negative in the measured distribution. These results show that reactant gases in smaller pockets are more likely to be consumed at a rate of 1.13 m/s, whereas, larger pocket reactant gases

are more likely to be consumed at a rate of 0.92 m/s. These differences may be due to flame curvature effects, although more data sets would be needed to confirm this result.

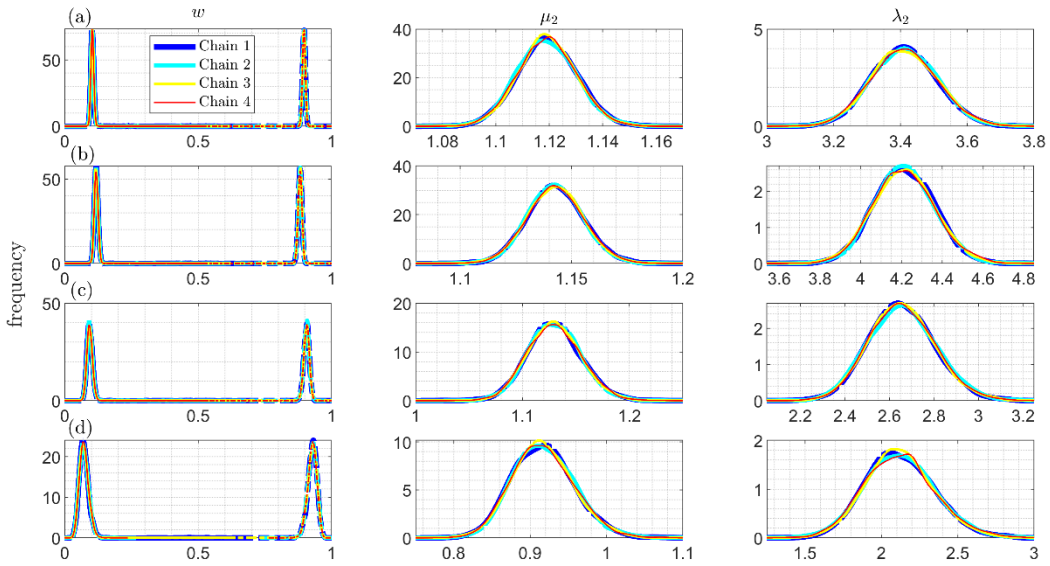

Figure 44. Probability densities of Markov chains for variables in the model: w, μ_2, λ_2 for (a) all pockets, (b) pockets with 0 mm < r_{mean} ≤ 2 mm, (c) pockets with 2 mm < r_{mean} ≤ 4 mm, (d) pockets with r_{mean} > 4mm

Table 5: Deconvolution PDF results

Case	μ_2	λ_2	$\hat{\pi}$
All pockets	1.11	3.18	0.91
0 mm < r_{mean} ≤ 2 mm	1.13	3.91	0.9
2 mm r_{mean} ≤ 4 mm	1.13	2.53	0.92
r_{mean} > 4mm	0.92	2	0.94

Figure 45 shows the log-likelihood probabilities of measured consumption rates belonging to distribution 2 (left column), with the scatter plot showing the measured data set and the color corresponding to the likelihood of the data point being in the deconvoluted distribution 2. These log-likelihoods,

$$\mathcal{L}_i = \log\left(w_k f_k(x_i)\right) \tag{10}$$

are dependent on the weights of each distribution and the distribution shape. A comparison of the shapes of distributions 1 and 2 shows that probabilities of consumption rates near zero are higher for distribution 1, when compared with distribution 2. For each observed sample, the log-likelihood values can be compared to categorize the sample to belong to either distribution 1 or 2:

$$z_i = \arg\max(\mathcal{L}) \tag{11}$$

Using Equation (11), it can be seen that a majority of the observed samples (as high as 91-95 %) have the likelihood of belonging to distribution 2, indicating that using the current approach, the estimated

percentage of out-of-plane consumption rates to be found in the measured consumption rates is relatively low (Figure 45). The interpretation of this result is that out-of-plane effects for pocket consumption rates are low in the current experimental measurements using the current model. Further comparison of the measured and true PDFs is shown in Figure 46, confirming these results and showing the final output of this methodology, which is a "true" PDF of pocket consumption rates.

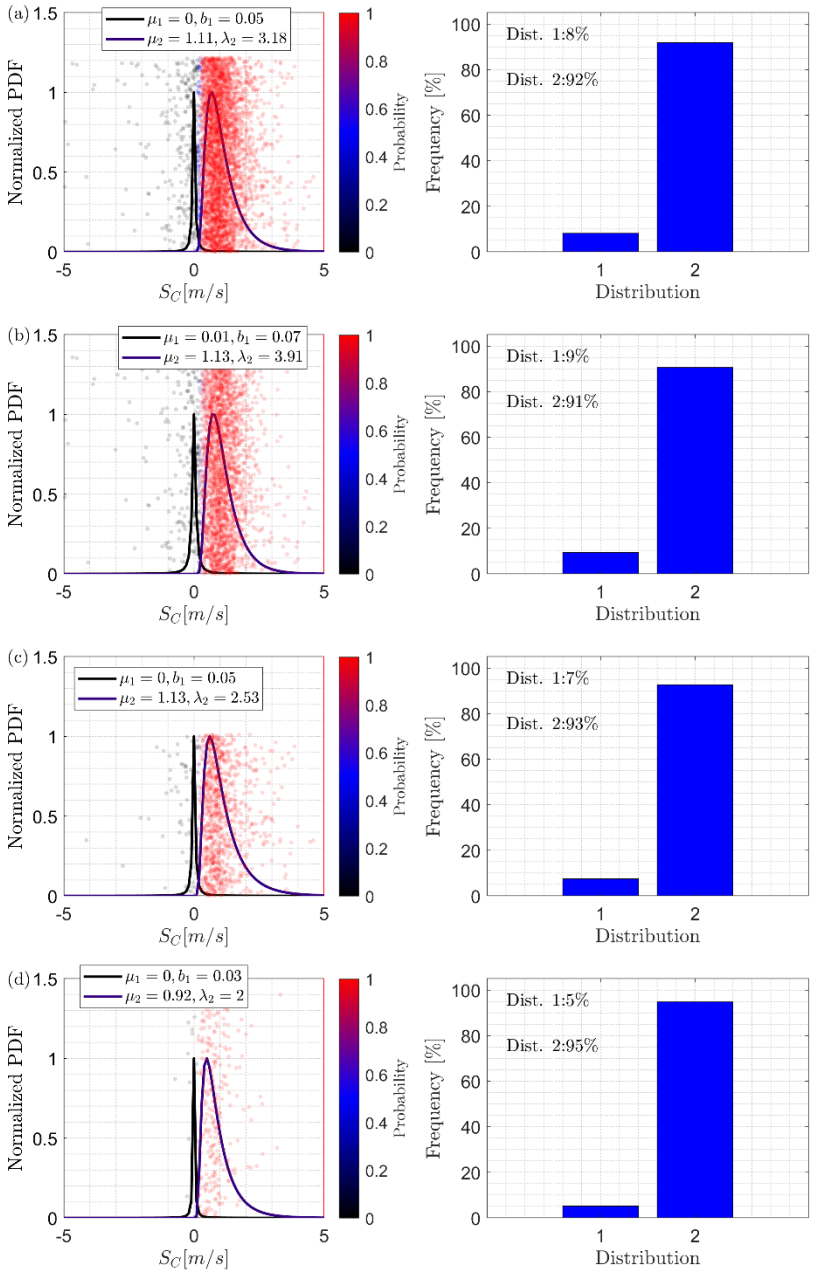

Figure 45. Deconvolution of out-of-plane consumption rate PDFs from measured PDFs for (a) all pockets, (b) pockets with 0 mm < $r_{mean} \leq$ 2 mm, (c) pockets with 2 mm < $r_{mean} \leq$ 4 mm, (d) pockets with r_{mean}> 4mm

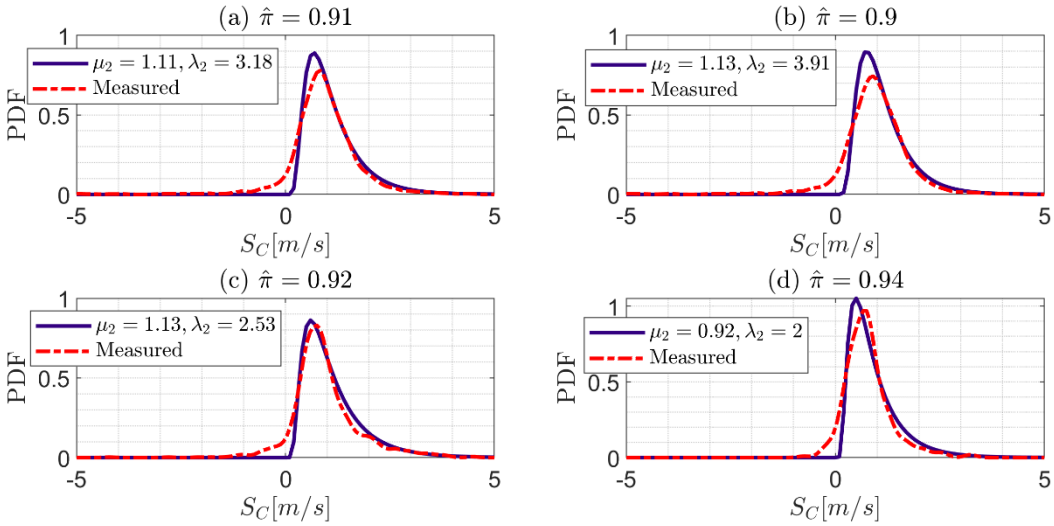

Figure 46. Comparisons between deconvoluted and measured PDFs for (a) all pockets, (b) pockets with 0 mm < $r_{mean} \leq$ 2 mm, (c) pockets with 2 mm < $r_{mean} \leq$ 4 mm, (d) pockets with r_{mean} > 4mm